

Young but fading radio sources: searching for remnants among compact steep-spectrum radio sources

M. Orienti^{1*}, M. Murgia², D. Dallacasa^{1,3}, G. Migliori¹, F. D’Ammando¹

¹INAF - Istituto di Radioastronomia, Via P. Gobetti 101, I-40129 Bologna, Italy

²INAF - Osservatorio Astronomico di Cagliari, Via della Scienza 5, I09047 Selargius, Italy

³Dipartimento di Fisica e Astronomia, Università di Bologna, Via Gobetti 93/2, I-40129 Bologna, Italy

Received 26 April 2023; accepted ?

ABSTRACT

The incidence of young but fading radio sources provides important information on the life cycle of radio emission in radio-loud active galactic nuclei. Despite its importance for constraining the models of radio source evolution, there are no systematic studies of remnants in complete samples of young radio sources. We report results on the study of 18 compact steep-spectrum (CSS) radio sources, selected from the statistically complete B3-VLA CSS sample, characterized by a steep optically-thin spectrum ($\alpha \geq 1.0$) and no core detection in earlier studies. Our deep multi-frequency Very Large Array (VLA), pc-scale Very Long Baseline Array (VLBA), and eMERLIN observations allowed us to locate the core component in 10 objects. In 3 CSS sources there is no clear evidence of present-time active regions, suggesting they are likely in a remnant phase. Among sources with core detection, we find 3 objects that have no clear active regions (hotspots) at the edges of the radio structure, suggesting that the radio emission may have just restarted. Our results support a power-law distribution of the source ages, although the poor statistics prevents us from setting solid constraints on the percentage of remnants and restarted sources in sub-populations of radio sources.

Key words: radio continuum: general - galaxies: active - radiation mechanisms: non-thermal

1 INTRODUCTION

Understanding how radio emission originates and evolves in extragalactic radio sources is one of the greatest challenges faced by modern astrophysics. The improvement in sensitivity recently achieved at radio wavelengths, together with the availability of multi-band information from infrared to gamma-ray observations is allowing a major step forward in our understanding of the physics of radio sources and the global properties of their host galaxies.

It appears that radio-loud active galactic nuclei (AGN) represent only a small fraction (about 10 per cent) of the total population of their host galaxies, suggesting that radio emission may be a transient phase in the lives of these systems. The typical duration of the active phase is 10^{7-8} yr, much shorter than the age of the host galaxy (Parma et al. 2007; Orrù et al. 2010; Harwood et al. 2017). Detection of dying radio emission implies that at some point the injection of relativistic plasma switches off and the radio emission rapidly fades due to energy losses

(Komissarov & Gubanov 1994; Murgia et al. 1999, 2011; Hardcastle 2018). For this reason, search for remnants is not an easy task in flux-density-limited catalogs (e.g. Slee et al. 2001; Parma et al. 2007), and many relics have been discovered serendipitously (e.g. Brienza et al. 2016; Randriamanakoto, Ishwara-Chandra & Taylor 2020).

After the radio emission has switched off, it is possible that a second epoch of radio activity starts. If the time elapsed is comparable, or longer than the radiative time of the outer lobes, only the new emission could be visible precluding us to identify the radio source as a restarted object. On the other hand, if the time elapsed between two consecutive episodes of radio emission is about 10 per cent of the total source age, we observe double-double radio sources (e.g., Lara et al. 1999; Schoenmakers et al. 2000; Konar et al. 2006). Radio sources showing more than two activity periods are very rare (Brocksopp et al. 2007; Hota et al. 2011; Singh et al. 2016). However, remnants and restarted objects are key to understand the life cycle of the radio emission and how active and quiescent periods are interleaved (Morganti 2017).

Systematic studies of remnants and restarted sources

* E-mail: orienti@ira.inaf.it

have been recently boosted mainly at low frequencies, thanks to the availability of high-sensitivity deep-field observations (e.g. Saripalli et al. 2012; Hardcastle et al. 2016; Brienza et al. 2017; Godfrey, Morganti & Brienza 2017; Mahatma et al. 2018; Hardcastle et al. 2019; Mahatma et al. 2019; Jurlin et al. 2020; Morganti et al. 2021; Jurlin et al. 2021). The relatively high fraction of remnants and restarted objects found in these works requires a dominant population of short-lived radio sources (Shabala et al. 2020).

There are indications that a significant fraction of compact steep spectrum (CSS) and peaked spectrum (PS) sources, which are radio sources in an early evolutionary stage (see e.g. O’Dea & Saikia 2021) will not be able to evolve into classical extended radio galaxies. First, there is a count excess of CSS/PS sources in flux-limited samples, which cannot be explained even when luminosity evolution is taken into account (e.g. O’Dea & Saikia 2021). Secondly, the age distribution estimated in a sample of CSS/PS sources peaks below 500 yr (Gugliucci et al. 2005). Finally, the fast evolution of the radio spectrum that we observe in some PS candidates suggests that not all the objects would become classical Fanaroff-Riley radio sources (Orienti & Dallacasa 2020). To explain these short-lived objects, Czerny et al. (2009) suggested a radiation pressure instability scenario which may cause an intermittent activity of the central engine: outbursts of radio emission, with a duration of 10^{3-4} years, repeat regularly every 10^{5-6} years. The detection of quasars that have transitioned from radio-quiet to radio-loud state on decadal time, may provide another indication that intermittent episodes of short-lived radio emission may be common in AGN (Nyland et al. 2020). Extended arcsecond scale radio emission (i.e. tens to hundred kpc and ages of 10^{7-8} yr) likely associated with young radio sources has been found only in a handful of PS objects (Stanghellini et al. 2005; Tinti et al. 2005). However, the discovery of relics from previous radio activities at parsec-scale distance from the young radio sources J1511+0518 (Orienti & Dallacasa 2008), and OQ 208 (Luo et al. 2007), suggests that the intermittency of short-lived active phases may have duty cycles of the order of 10^{3-4} yr. If the distribution of the source age follows a power-law as suggested by Shabala et al. (2020), one would expect a larger incidence of remnants among compact symmetric objects (CSOs), i.e. sources with linear size (LS) $\lesssim 1$ kpc, rather than middle-sized symmetric objects (MSOs), i.e. objects with $1 \text{ kpc} \lesssim \text{LS} \lesssim 20 \text{ kpc}$ ¹.

So far, not many studies searching for young but dying objects have been carried out (e.g., Kunert-Bajraszewska & Marecki 2007), and only a handful of young but fading sources are known (e.g., Orienti, Murgia & Dallacasa 2010; Callingham et al. 2015; O’Sullivan et al. 2021).

In this paper we aim at inferring, for the first time, the fraction of remnants in a complete sample of CSS radio sources. This will allow us to investigate the incidence of short-lived objects and to shed a light on the life cycle of the radio emission in its early evolutionary stages after the

outburst. Multi-frequency very large array (VLA), very long baseline array (VLBA), and eMERLIN observations of the target sources were performed in order to constrain the synchrotron radio spectrum and unveil the presence of active cores that may have been missed in previous observations with lower sensitivity.

The paper is organized as follows: in Section 2 we present the source sample, in Section 3 we describe the radio observations. Results are presented in Section 4 and discussed in Section 5. In Section 6 we draw our summary.

Throughout this paper, we assume the following cosmology: $H_0 = 70 \text{ km/s Mpc}^{-1}$, $\Omega_M = 0.27$ and $\Omega_\Lambda = 0.73$, in a flat Universe. The spectral index α is defined as $S(\nu) \propto \nu^{-\alpha}$.

2 THE SAMPLE

To look for young but fading sources we constructed a complete sample of candidate remnants from the B3-VLA CSS sample (Fanti et al. 2001). The B3-VLA CSS sample consists of 87 CSS/PS sources with flux density $> 0.8 \text{ Jy}$ at 0.4 MHz, a steep radio spectrum ($\alpha_{4.8}^{8.4} \gtrsim 0.7$), and an angular size $\lesssim 2 \text{ arcsec}$ (i.e. linear size $\lesssim 20 \text{ kpc}$). Multi-frequency VLA and VLBA observations were performed to study the radio structure: 25 out of the 87 sources of the sample with largest angular scale (LAS) $< 0.25 \text{ arcsec}$ were target of VLBA observations (Dallacasa et al. 2002a; Orienti et al. 2004), whereas the remaining 62 sources were target of VLA, EVN and MERLIN observations (Fanti et al. 2001; Dallacasa et al. 2002b; Rossetti et al. 2006).

Among the sources of the B3-VLA CSS sample we selected all the objects with a spectral index $\alpha_{4.8}^{8.4} > 1.0$ and without any core detection in earlier observations (Fanti et al. 2001; Dallacasa et al. 2002a,b; Orienti et al. 2004; Rossetti et al. 2006). We end up with a sample of 18 CSS sources: 6 with $\text{LAS} < 0.25 \text{ arcsec}$, and 12 with $\text{LAS} > 0.25 \text{ arcsec}$. The former were target of VLBA observations while the latter of VLA observations. For 6 of them we also got high-resolution eMERLIN observations. We complement our observations with archival high angular resolution VLA observations already published in Fanti et al. (2001) and Rossetti et al. (2006).

The source sample and the source properties are reported in Table 1².

3 RADIO OBSERVATIONS

3.1 VLA observations

Multi-frequency VLA observations of the 12 CSS sources with $\text{LAS} > 0.25 \text{ arcsec}$ ($\text{LS} > 1 \text{ kpc}$) were carried out during four runs between 2015 and 2017 (Table 2). Observations were performed in L (1–2 GHz) and S (2–4 GHz) bands with the array in A-configuration, while observations in U band (13–15 GHz) were performed with the array in B-configuration. The average angular resolution is about

¹ For details on the populations of CSOs and MSOs see the review by O’Dea & Saikia (2021)

² We still consider MSOs the three sources with LS between 20 and 30 kpc.

Table 1. The source sample. Column 1: source name; column 2: optical identification (G = galaxy; E: empty field); column 3: redshift (p = photometric redshift); columns 4 and 5: flux density at 4.8 and 8.4 GHz, respectively, from Fanti et al. (2001); column 6: spectral index between 4.8 and 8.4 GHz; column 7: angular size from Fanti et al. (2001); column 8: projected linear size. When the redshift is unknown we assume $z=1.05$ (see, Fanti et al. 2001); column 9: reference for the redshift: 1: Thompson et al. (2000); 2: Fanti et al. (2001); 3: Jarvis et al. (2001); 4: Cruz et al. (2006); 5: Pahre & Djorgovski (1995); 6: Fanti et al. (2011); 7: Allington-Smith et al. (1988); 8: Thompson et al. (1994); 9: Rawlings, Eales & Lacy (2001); 10: Wegner et al. (2003); 11: Sloan Digital Sky Survey Data Release 13 (Albareti et al. 2017).

Source Name	ID	z	$S_{4.8\text{GHz}}$ mJy	$S_{8.4\text{GHz}}$ mJy	$\alpha_{4.8}^{8.4}$	LAS arcsec	LS kpc	Ref.
B3-0003+387	G	1.47	52.8	22.4	1.4	1.3	11.2	1
B3-0034+444	G	2.79	187.7	96.5	1.0	3.2	25.6	2
B3-0128+394	G	0.929	128.9	42.8	1.1	2.7	21.5	3
B3-0140+387	G	2.9p	71.0	27.5	1.5	0.7	5.5	2
B3-0748+413B ^a	E	-	42.5	23.4	1.2	0.4	3.2	-
B3-0754+396 ^a	G	2.119	143.1	74.7	1.1	2.2	19.6	2
B3-0810+460B	G	0.620	466.4	153.9	1.1	0.63	4.3	4
B3-0856+406	G	2.285	37.8	14.0	1.5	0.8	6.7	5
B3-1016+443	G	0.7p	80.1	39.3	1.2	0.11	0.7	6
B3-1039+424 ^a	E	-	66.2	32.3	1.1	1.5	12.2	-
B3-1049+384	G	1.018	200.6	104.9	1.1	0.1	0.8	7
B3-1133+432	E	-	499.1	286.3	1.0	0.07	0.5	-
B3-1143+456	G	0.762	137.1	64.7	1.4	0.8	6.0	8
B3-1212+380	G	0.947	63.8	33.3	1.2	0.3	2.4	9
B3-1216+402	G	0.756	161.6	61.5	1.0	3.8	28.3	8
B3-1225+442	G	0.348	96.3	45.7	1.2	0.2	1.0	10
B3-1340+439	E	-	130.4	67.0	1.2	0.07	0.5	-
B3-1449+421	G	0.86p	147.4	66.5	1.6	0.08	0.6	11

^aSource re-classified as a large symmetric object.

1.2 arcsec, 0.6 arcsec, and 0.5 arcsec in L, S, and U bands, respectively. L-band observations have a bandwidth of 1 GHz, whereas observations in S and U bands have a bandwidth of 2 GHz. In each frequency band the bandwidth was divided into 16 spectral windows. Depending on the local sidereal time range of the observing runs, either 3C 48 or 3C 286 was used as primary, band pass, and electric vector position angle (EVPA) calibrator. Each source was observed for about 8 min per frequency. Secondary calibrators were chosen to minimize the antenna slewing. In two observing runs (15A-140 in L and S bands, and 16B-107 in U band) we observed as secondary calibrators J0713+4349 and J0111+3906, respectively, which we also used as leakage (D-term) calibrators.

Calibration was performed using the **CASA** software (McMullin et al. 2007) following the standard procedure for the VLA. Parts of L and S bands were highly affected by RFI. In particular in L band we had to fully flag some spectral windows. Errors on the amplitude calibration are conservatively 3 per cent in L and U bands, and 5 per cent in S band. After the a-priori calibration, imaging was done with the **CASA** task **TCLEAN**. When other objects were present in the field of view, mainly in L-band, we made use of the task **CLEAN** which allows imaging with several phase centers.

Few iterations of imaging and self-calibration were performed before creating the final images, which were produced with Briggs weighting and using Multi-frequency synthesis algorithm with 2 Taylor terms. Flux densities were measured using the **CASA** task **IMFIT** which per-

forms a Gaussian fit on the image plane. If the source (source components) could not be fitted by a Gaussian, we extracted the flux density on a selected polygonal area using the **CASA** task **VIEWER**. In Table 3 we report the flux densities at 1.4, 3 and 14 GHz. To maximize the spectral coverage, we produced an image for each spectral window (see Section 4.1). Errors on the flux densities are estimated by $\sigma = \sqrt{\sigma_{\text{cal}}^2 + \sigma_{\text{fit}}^2 + \sigma_{\text{rms}}^2}$, where σ_{cal} is the uncertainty on the amplitude calibration, σ_{fit} is the error on the Gaussian fit, and σ_{rms} is the 1- σ noise level measured on the image plane, which is $\sigma_{\text{rms}} = \text{rms} \times \sqrt{\theta_{\text{source}}/\theta_{\text{beam}}}$, where θ_{source} is the source area, and θ_{beam} is the area of the Gaussian restoring beam.

Final images of the CSS sources are presented in Fig. A1, while images of the sources falling within the VLA field of view showing a resolved structure are presented in Fig. B1. Properties of field sources are reported in Table B1.

3.2 VLBA observations and data reduction

VLBA observations in C and X bands of the CSS sources with $\text{LAS} < 0.25$ arcsec were carried out between 2010 December and 2011 January in dual polarization (Table 2) at 32-MHz bandwidth, with the exception of B3-1133+432 (both bands) and B3-1049+384 (C band only) whose data were already published in Orienti et al. (2004).

Each source was observed for about 2 hr spread into twelve 10-min scans. No fringes were detected for B3-1225+442 in C band. Calibration and data reduction were

Table 2. Log of radio observations. Column 1: date of observation; column 2: project code; column 3: array; column 4: observing band; column 5: polarization calibration.

Date	Project	Array	Band	Polarization
2015-02-15	15A-140	VLA-B	U	Y
2015-08-14	15A-140	VLA-A	L,S	N
2017-01-06	16B-107	VLA-A	L,S	Y
2017-10-19	17B-153	VLA-B	U	N
2010-12-31	BO038A	VLBA	C,X	N
2011-01-16	BO038C	VLBA	C,X	N
2011-01-21	BO038B	VLBA	C,X	N
2020-08-03/09	CY10208	eMERLIN	L,C	N

performed following the standard procedures described in the Astronomical Image Processing System (AIPS) cookbook. J0927+3902 was used to generate the band pass correction. Amplitudes were calibrated using antenna system temperatures and antenna gains. Uncertainties on the amplitude calibration are approximately 10 per cent at both frequencies.

Images were produced in AIPS with the task IMAGR. Few iterations of imaging and phase-only self-calibration were performed before producing final images. In addition to full-resolution images, we produced a set of images in C and X bands with the same uv -range, beam size, and pixel size, with the aim of computing the spectral index. Flux densities were measured using TVSTAT in AIPS which allows the selection of a polygonal region on the image plane. VLBA images are shown in Fig. A2, while flux densities and spectral indexes are reported in Table 4. Errors on the flux density are computed using the formula reported in Section 3.1, while errors on the spectral index are computed assuming the error propagation theory.

3.3 eMERLIN observations

eMERLIN observations were carried out between 3 and 9 August 2020 in L and C bands. The target sources were observed for about 4 and 3.5 hr in L and C bands, respectively. Initial flagging and data calibration were done using the eMERLIN CASA pipeline. After the a-priori calibration some data were still highly affected by RFI, especially in L-band, and additional flagging was done before starting the imaging process. Final images were produced after a few self-calibration iterations and are reported in Fig. A3. In addition to the *full-resolution* images, we also produced a set of *low-resolution* images with uv -range (50–1250 k λ), pixel size and restoring beam common to L and C bands. These images were used to estimate the spectral index between L and C bands. Owing to the severe flagging, the final rms of the L-band images is of a few mJy beam⁻¹, much worse than the planned rms.

Flux densities are reported in Table 5 and were measured with the same CASA tasks described for the analysis of VLA data (see Section 3.1). Errors on the flux density are

computed using the formula reported in Section 3.1.

4 RESULTS

4.1 Spectral fit

For the sources observed with the wide bandwidth available at the VLA we measured the flux density for each spectral window, in order to exploit the spectral coverage as much as possible. Flux densities at 4.8 and 8.4 GHz are from historical VLA observations with narrow bandwidth (Fanti et al. 2001). Flux densities in U band are from our new low-resolution wide band observations which guarantee a better characterization of the high frequency part of the spectrum, preventing the artificial steepening that may be caused by the lack of short spacings of earlier high resolution observations (Rossetti et al. 2006), unable to pick up extended low-surface brightness emission.

For the compact sources targeted by VLBA observations we constructed the integrated radio spectrum making use of VLA flux density from the literature where the sources are unresolved. This prevents us to miss flux density that may be resolved out and/or poorly sampled in our VLBA observations.

We complemented the information in the GHz regime by including flux density at 74 MHz from the VLA low-frequency sky survey (VLSS; Cohen et al. 2007) and VLSS redux (Lane et al. 2014), 150 MHz from the TIFR GMRT sky survey (TGSS; Intema et al. 2017), and at 408 MHz (Ficarra, Grueff & Tomassetti 1985) in order to characterize the radio spectrum at low frequencies.

To determine the shape of the synchrotron emission we fit the radio spectrum of the sources assuming two different models. The first model implies a continuous injection of fresh relativistic particles (CI model), while in the second one the injection of new particles has switched off and the source is already in a relic phase (CI OFF model). In the latter model a second break appears in the spectrum at high frequencies and beyond that the spectrum cuts off exponentially. In both models radiative losses dominate over the other energy losses (see Murgia 2003) and are characterized by a) the injection spectral index (α_{inj}), b) the break frequency (ν_b), c) and the flux normalization. In addition to these parameters, the CI OFF model is also characterized by the relic to total source age ratio (t_{OFF}/t_s , i.e. the relic period and the source age, respectively). For $t_{OFF} \rightarrow 0$, CI OFF model approaches CI model³.

When the turnover frequency falls within the frequency range covered by the observations, we fit the optically-thick part of the spectrum with a pure synchrotron self-absorption

³ In addition to the CI/CI OFF models, we fitted the spectrum considering a passive evolution of a synchrotron spectrum without any injection of fresh particles and either with a continuous re-isotropization of the pitch angle (JP, Jaffe & Perola 1973) or without (KP, Kardashev 1962). Both models are usually comparable and their χ^2_{red} is in good agreement with that of CI OFF model, since the CI OFF model tends to the JP for $t/t_{OFF} \rightarrow 1$.

Table 3. Multi-frequency VLA flux density of CSS sources with $\text{LAS} > 0.25$ arcsec. Column 1: source name; column 2: source component; columns 3-5: flux density (in mJy) at 1.4, 3, and 14 GHz, respectively; column 6: spectral index between 3 and 14 GHz.

Source (1)	Comp. (2)	$S_{1.4}$ (3)	S_3 (4)	S_{14} (5)	$\alpha_{3\text{GHz}}^{14\text{GHz}}$ (6)
B3-0003+387	N	262.8 ± 7.9	114.5 ± 3.4	11.3 ± 0.4	1.5 ± 0.1
	S	227.0 ± 6.8	108.8 ± 3.3	12.4 ± 0.4	1.4 ± 0.1
	Tot	487.4 ± 14.6	214.6 ± 6.4	23.4 ± 0.7	1.4 ± 0.1
B3-0034+444	N	581.8 ± 17.5	314.3 ± 9.4	56.1 ± 1.7	1.1 ± 0.1
	S	99.1 ± 6.0	26.4 ± 0.8	2.0 ± 0.1	1.7 ± 0.1
	A	-	243.6 ± 7.5	51.8 ± 1.5	1.1 ± 0.2
	B	-	45.1 ± 2.7	4.8 ± 0.2	1.6 ± 0.2
	C	-	9.3 ± 1.7	1.1 ± 0.2	1.4 ± 0.2
	D	-	17.8 ± 2.0	1.0 ± 0.2	1.9 ± 0.2
	Tot	707.8 ± 21.2	347.6 ± 10.4	58.1 ± 1.7	1.2 ± 0.1
B3-0128+394	N	173.2 ± 5.4	86.4 ± 4.0	13.4 ± 0.5	1.2 ± 0.1
	S	163.0 ± 5.1	75.5 ± 4.0	11.2 ± 0.6	1.2 ± 0.1
	Tot	334.3 ± 10.0	162.1 ± 4.9	25.0 ± 0.8	1.2 ± 0.1
B3-0140+387	N	-	90.6 ± 2.7	6.3 ± 0.2	1.7 ± 0.1
	S	-	77.2 ± 2.3	7.9 ± 0.3	1.5 ± 0.1
	Tot	450.2 ± 13.6	167.1 ± 5.0	14.0 ± 0.4	1.6 ± 0.1
B3-0748+413B	N	200.3 ± 6.1	83.5 ± 4.4	13.6 ± 0.5	1.2 ± 0.1
	C	2.9 ± 0.2	1.5 ± 0.3	0.7 ± 0.1	0.6 ± 0.1
	S	20.5 ± 1.2	9.1 ± 0.7	2.6 ± 0.2	0.9 ± 0.2
B3-0754+396	Tot	231.7 ± 7.0	94.1 ± 4.9	17.6 ± 0.5	1.1 ± 0.1
	N	525.7 ± 15.8	247.8 ± 13.1	45.7 ± 1.4	1.1 ± 0.1
	S	7.8 ± 0.3	3.4 ± 0.3	0.5 ± 0.1	1.2 ± 0.1
B3-0810+460B	Tot	533.5 ± 16.0	251.2 ± 13.3	46.2 ± 1.5	1.1 ± 0.1
	N	-	216.1 ± 10.8	35.0 ± 1.1	1.2 ± 0.1
	S	-	276.6 ± 13.8	54.9 ± 1.6	1.1 ± 0.1
B3-0856+406	Tot	1146.5 ± 34.3	492.7 ± 24.6	90.9 ± 2.8	1.1 ± 0.1
	E	-	54.3 ± 3.1	4.2 ± 0.2	1.7 ± 0.1
	W	-	26.3 ± 1.5	3.8 ± 0.2	1.3 ± 0.1
B3-1039+424	Tot	225.5 ± 6.8	80.6 ± 4.5	7.7 ± 0.3	1.6 ± 0.1
	N	7.5 ± 0.5	2.7 ± 0.3	0.4 ± 0.1	1.3 ± 0.1
	C	0.2 ± 0.1	0.15 ± 0.03	0.05 ± 0.02	0.4 ± 0.7
B3-1143+456	S	273.6 ± 8.2	118.2 ± 6.5	17.8 ± 0.6	1.3 ± 0.1
	Tot	281.1 ± 8.4	120.9 ± 6.6	18.0 ± 0.6	1.3 ± 0.1
	N	-	45.8 ± 2.6	4.2 ± 0.2	1.6 ± 0.1
B3-1212+380	S	-	230.8 ± 12.0	27.8 ± 0.8	1.4 ± 0.1
	Tot	693.6 ± 23.8	276.6 ± 13.8	31.8 ± 1.1	1.5 ± 0.1
	Tot	304.6 ± 9.1	121.6 ± 6.1	17.5 ± 0.6	1.3 ± 0.1
B3-1216+402	N	155.3 ± 4.7	71.5 ± 4.0	14.4 ± 0.4	1.1 ± 0.1
	S	211.4 ± 6.3	107.2 ± 5.4	22.3 ± 0.7	1.0 ± 0.1
	Tot	364.3 ± 10.9	178.7 ± 9.0	37.2 ± 1.1	1.0 ± 0.1

(SSA) model ($\alpha_{\text{thick}} = 2.5$). A detailed description of the spectral models can be found in [Murgia et al. \(2011\)](#).

To evaluate the best model that fits the spectrum we compare the value of the injection spectral index and the reduced chi-square. An example of the fits for B3-0003+387 is shown in Fig. 1. Fits of the overall spectra for the whole sample are presented in Fig. C1, and the parameters are reported in Table C1.

4.2 Polarization

For the sources observed with the VLA we could study the polarization either in L-S bands or in U band. In all the sources we detect polarized emission with the exception of B3-1143+456 and B3-1212+380 which are unpolarized

(polarization percentage $m < 0.1$ per cent) in both L and S bands, and B3-0003+387, unpolarized in U band ($m < 0.5$ per cent). To estimate the rotation measure (RM) we complemented our data with the information in C and X bands from [Fanti et al. \(2001\)](#). In three sources (B3-0003+387, B3-0034+444, and B3-1216+402) we find $|\text{RM}| > 100 \text{ rad m}^{-2}$, whereas in B3-0748+413B, B3-0754+396, and B3-1039+424, $|\text{RM}| < 12 \text{ rad m}^{-2}$, consistent with the Galactic value ([Taylor, Stil & Sunstrum 2009](#)). The latter sources are also those showing the highest polarization percentage $m \gtrsim 10$ per cent. Our deep VLA observations point out that these objects are components of larger sources which extend far beyond the host galaxy, and therefore are not genuine CSS sources (see Section 4.3).

For some objects our RM differs from those reported in [Rossetti et al. \(2008\)](#) and this is likely due to the lower resolution of the WSRT data (8 arcsec) which could not

Table 4. VLBA flux density of the CSS sources with $\text{LAS} < 0.25$ arcsec. Column 1: source name; column 2: source component; columns 3 and 4: flux density at 4.8 and 8.3 GHz, respectively; column 5: spectral index between 4.8 and 8.3 GHz (see Section 3.2). For the source B3-1049+384 the flux density at 4.8 GHz is measured on the image from [Orienti et al. \(2004\)](#). For B3-1225+442 the spectral index is computed between 1.7 GHz ([Dallacasa et al. 2002a](#)) and 8.3 GHz.

Name	Comp.	S _{4.8} mJy	S _{8.3} mJy	$\alpha_{4.8}^{8.3}$
B3-1016+443	N	45.4±4.6	18.7±1.9	1.6±0.3
	S	6.6±1.0	-	-
	Tot	52.0±5.2	18.7±1.9	-
B3-1049+384	W1	74.6±7.5	33.9±3.4	1.3±0.3
	W2	83.8±8.4	51.5±5.2	0.9±0.3
	C	15.1±1.5	19.0±1.9	-0.4±0.3
	E	4.2±0.5	2.2±0.3	1.2±0.3
	Tot	180.7±18.1	106.6±10.7	1.0±0.3
B3-1225+442	W1A	-	7.1±0.7	0.1±0.1
	W1B	-	2.4±0.2	0.6±0.1
	E	-	8.6±1.0	-
	Tot	-	18.1±1.9	-
B3-1340+439	N1	84.7±8.5	29.7±3.0	1.2±0.3
	N2	20.6±2.1	13.6±1.4	0.9±0.3
	C	8.0±0.9	6.4±0.7	0.4±0.3
	S	8.6±0.9	2.6±0.4	-
	Tot	124.8±12.5	52.3±5.3	-
B3-1449+421	N	66.5±6.6	21.5±2.2	1.7±0.3
	C	8.1±1.0	5.0±0.5	0.9±0.3
	S3	14.3±1.5	5.2±0.6	1.7±0.3
	S2	21.0±2.1	11.5±1.2	0.9±0.3
	S1	22.2±2.2	5.7±0.7	-
	Tot	132.4±13.3	48.8±5.0	-

Table 5. eMERLIN flux density of CSS sources. Column 1: source name; column 2: source component; columns 3 and 4: flux density at 1.5 and 4.8 GHz, respectively, measured on the *full-resolution* images; column 5: spectral index between 1.5 and 4.8 GHz, computed using images constructed with the same *uv*-range, pixel size and restoring beam (see Section 3.3).

Name	Comp.	S _{1.5} mJy	S _{4.8} mJy	$\alpha_{1.5}^{4.8}$
B3-0003+387	N	221.9±11.2	29.8±1.5	1.7±0.1
	S	171.0±8.8	32.9±1.7	1.4±0.1
	Tot	392.9±19.6	62.7±3.1	1.6±0.1
B3-0140+387	N	211.4±10.6	11.0±0.6	1.8±0.1
	C	52.8±2.9	3.7±0.5	1.7±0.1
	S1	88.4±4.4	4.7±0.5	1.9±0.1
	S2	15.2±1.3	-	-
B3-0810+460B	Tot	371.0±18.6	19.4±1.0	1.9±0.1
	N	439.4±22.0	79.7±4.0	1.2±0.1
	S1	258.9±13.1	59.1±3.0	1.1±0.1
	S2	262.5±13.5	11.7±5.2	1.4±0.2
B3-0856+406	Tot	943.0±47.2	150.5±7.6	1.3±0.2
	E	154.1±7.8	13.5±0.7	1.8±0.1
	C	-	1.0±0.3	-
	W	46.2±2.4	5.1±0.3	1.4±0.1
B3-1143+456	Tot	202.8±10.4	19.6±1.0	1.7±0.1
	N	115.2±6.8	7.0±1.1	2.4±0.1
	S	526.8±26.6	64.8±3.4	1.8±0.1
	Tot	628.3±32.0	71.8±3.6	1.9±0.1
B3-1212+380	N	138.0±7.0	18.9±1.0	1.5±0.1
	S	137.3±7.0	14.0±0.7	1.5±0.1
	S1	-	5.1±0.3	-
	S2	-	8.9±0.6	-
	Tot	275.3±13.8	32.9±1.7	1.5±0.1

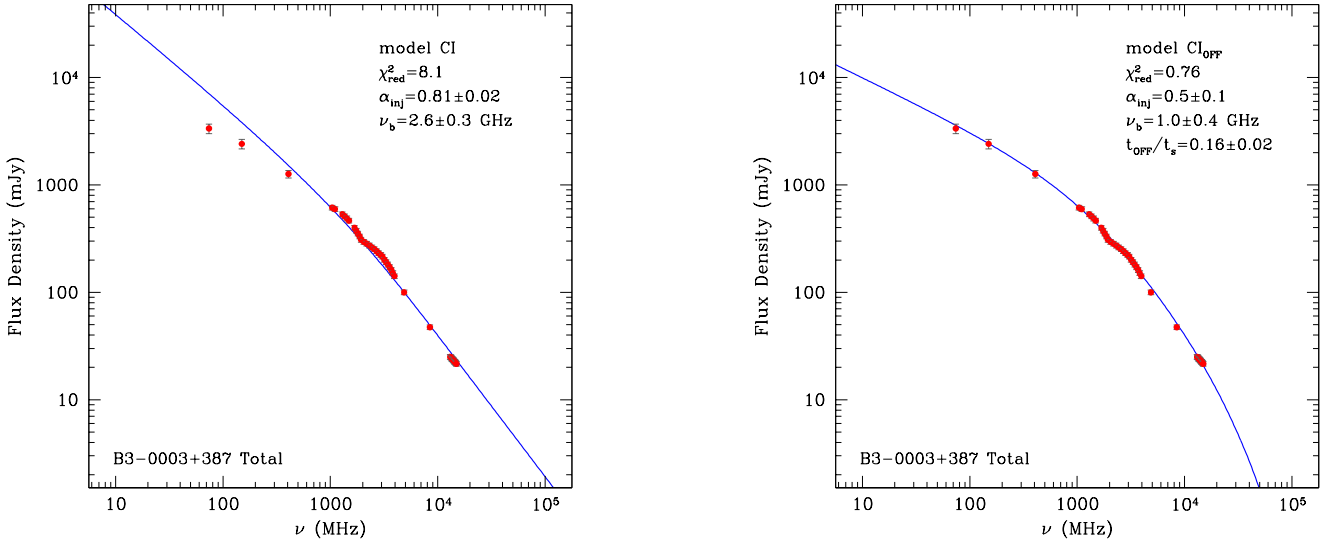


Figure 1. Integrated spectrum of the source B3-0003+387 along with the best-fit CI model (*left*) and best-fit CI OFF model (*right*).

resolve the polarized emission from different components, implying some level of beam depolarization.

4.3 Notes on individual sources

Here we provide a brief description of the sources, and their classification: active, remnant, restarted, large symmetric object (LSO). The classification is based on the detection, or not, of active regions, like core and hotspots, and results from the synchrotron fit to the integrated spectrum. A question mark indicates that the information is not adequate for a secure classification of the radio emission.

In general, the spectral indices were computed using the flux densities measured on images that were produced using a uv -range, image sampling, and restoring beam common to both frequencies. For VLA data, we report the spectral index between 3 and 14 GHz, since the structure of many sources is unresolved or marginally resolved at 1.4 GHz. For some sources with eMERLIN observations, in addition to the spectral index between 1.7 and 4.8 GHz from the eMERLIN data sets, we also computed the spectral index using the 4.8-GHz eMERLIN data and the high-resolution 15-GHz VLA data from Rossetti et al. (2006). The use of these data sets obtained with different arrays may affect the determination of the spectrum, mainly for extended structures. Therefore, we provide the spectral index using the 4.8-GHz eMERLIN data and the high-resolution 15-GHz VLA data only for compact regions.

VLA images of the sources are shown in Fig. A1: contours show total intensity emission, while polarized emission (and E-vectors) are shown in colors (for data sets with available polarization information). Total intensity images from VLBA observations are shown in Fig. A2, while eMERLIN images are presented in Fig. A3.

4.3.1 B3-0003+387 - remnant

The source has a double structure with no evidence of the source core. Both components, unresolved with the VLA, have a steep spectral index ($\alpha > 1.0$, Tables 3 and 5) and are elongated in the C-band eMERLIN image, with no evidence of any compact region. No significant total-intensity flux-density asymmetry between the two components is observed. The polarized emission is highly asymmetric, with the southern component showing a fractional polarization of about 6.5 per cent and an RM of -135 rad/m^2 , while the northern component is unpolarized. The radio spectrum is well reproduced by CI OFF model (Fig. 1), supporting the relic nature of this object. This source is one of the two objects best fitted by a JP model in Rossetti et al. (2006). The time spent by the source in the relic phase is about 16 per cent of the total radio source age.

4.3.2 B3-0034+444 - active?

The source has an elongated morphology that reminds of a jetted structure. There is no clear evidence for a flat-spectrum core component. Rossetti et al. (2006) suggested component B as the candidate core based on their high resolution 15-GHz data. However, from our VLA data this component shows a rather steep spectrum ($\alpha_3^{14} \sim 1.6$), while component A, edge-brightened in the 15-GHz images presented in Rossetti et al. (2006), has a spectral index of 1.1. Components C and D are resolved out in the high-resolution 15-GHz images (Rossetti et al. 2006), suggesting the lack of compact regions. At 14 GHz only components A and B are polarized. Both CI and CI OFF models provide a similar fit to the spectrum. Since t_{OFF} is very short, the CI OFF model is rather equivalent to the CI model (see Section 4.1). The result from the spectral analysis together with the information on the source structure pointed out

Table 6. Polarization properties. Column 1: source name; column 2: source component; columns 3 and 4: polarization percentage and polarization angle in L band, respectively; columns 5 and 6: polarization percentage and polarization angle in S band, respectively; columns 7 and 8: polarization percentage and polarization angle in U band, respectively; column 9: rotation measure; column 10: intrinsic polarization angle.

Source name	Comp.	m_L %	χ_L deg	m_S %	χ_S deg	m_U %	χ_U deg	RM rad/m ²	χ_0 deg
B3-0003+387	N	-	-	-	-	<0.5	-	-	-
	S	-	-	-	-	6.5	23±4	-135	26
B3-0034+444	A	-	-	-	-	4.3	14±7	109	11
	B	-	-	-	-	4.0	-47±2	-	-
B3-0128+394	N	-	-	-	-	2.9	-62±5	-	-
	S	-	-	-	-	4.7	-60±5	-	-
B3-0140+387	N	-	-	-	-	2.5	66±2	-	-
	S	-	-	-	-	5.0	-50±2	-	-
B3-0748+413B	N	0.1	-44±4	2.4	-38±8	-	-	-4	-34
	S	11.7	42±4	16.2	13±3	-	-	-	-
B3-0754+396	N	8.0	85±8	9.8	84±8	-	-	2	81
	S	<0.1	-	3.6	28±8	-	-	-	-
B3-0810+460B	W	<0.1	-	0.1	0±2	-	-	-	-
B3-0856+406	Tot	<0.1	-	<0.1	-	-	-	-	-
B3-1039+424	N	5.6	36±4	14.1	17±4	-	-	-	-
	S	7.0	-49±2	13.8	-67±2	-	-	12	-76
B3-1143+456	Tot	<0.1	-	<0.1	-	-	-	-	-
B3-1212+380	Tot	<0.1	-	<0.1	-	-	-	-	-
B3-1216+402	N	0.6	73±5	8.5	77±4	-	-	-5	84
	S	0.2	49±6	1.8	-42±8	-	-	-151	41

by high-resolution images make us conservatively consider B3-0034+444 as a candidate active source.

4.3.3 B3-0128+394 - active?

Source with a double structure characterized by a mildly steep spectrum ($\alpha_3^{14} \sim 1.2$) and no significant flux-density asymmetry. There is no clear evidence for a flat-spectrum core component. In the high resolution images presented in Rossetti et al. (2006) the extended structure of both the northern and southern components is resolved out and only the hotspots are detected and resolved in sub-structures. In particular, the compact component in the northern lobe has a rather flat spectral index $\alpha_{8.5}^{15} \sim 0.5$ when super-resolved images at 8.5 GHz are considered (Rossetti et al. 2006). At 14 GHz the peak of polarized emission in the northern component does not coincide with the peak of total-intensity emission, but it is centered on the component labelled N2 in Rossetti et al. (2006). Both CI and CI OFF models provide a similar fit to the spectrum, with the latter slightly preferred over the former. The result from the spectral analysis together with the information on the source structure, i.e. presence of hotspots but lack of clear core detection make us conservatively consider B3-0128+394 a candidate active source.

4.3.4 B3-0140+387 - active

Source showing a double structure in VLA images. When observed with the higher resolution of eMERLIN it shows a triple structure. If we compare the eMERLIN data at

4.8 GHz and the VLA data at 15 GHz from Rossetti et al. (2006) we find that the central component, labelled C in Fig. A3, has a relatively flat spectrum ($\alpha_{4.8}^{15} \sim 0.5$), indicating that it may host the source core. Similarly, the outer compact components labelled N and S1 in eMERLIN image (Fig. A3) have a spectral index $\alpha_{4.8}^{15} \sim 0.6$ and 0.7, respectively, i.e. much flatter than those derived by lower resolution data (Tables 3 and 5). However, when observed with the high resolution provided by the European Very Long Baseline Interferometry (VLBI) network (EVN) at 18 cm only two compact regions are detected at the edges of the source, while no compact component is clearly detected at the centre (Dallacasa et al. 2002b), suggesting that the core may be absorbed at such frequency. The steep spectrum derived from low-resolution data may be due to the contamination of steep-spectrum emission from lobes and jets, which is resolved out at high resolution. Component N is the brightest in total intensity, with a flux density ratio between N and S1 of about 2.3 and 2.5 in 4.8-GHz eMERLIN data and in 15-GHz high-resolution VLA data (Rossetti et al. 2006), respectively, while component S has the highest level of polarization (Table 6). Both SSA+CI and SSA+CI OFF models provide a similar fit to the spectrum. However, the detection of hotspots and the tentative identification of the core component suggest that the source is active.

4.3.5 B3-0748+413B - LSO

The source that was classified as a CSS in Fanti et al. (2001) turns out to be the northern lobe/hotspot, labelled N in Fig. A1, of a larger radio source with $LAS \sim 13.5$

arcsec ($LS \sim 110$ kpc assuming $z=1.05$). The radio source has an asymmetric structure with the core at about 4 arcsec from component N and about 9 arcsec from component S. The RM of component N is consistent with the Galactic value (Table 6) suggesting that the radio emission is not embedded within the interstellar medium (ISM) of the host galaxy. On the basis of these new pieces of evidence we classify B3-0748+413B as an LSO and remove it from the sample of CSS sources.

4.3.6 B3-0754+396 - LSO

The source that was classified as a CSS in Fanti et al. (2001) is likely the northern lobe/hotspot, labelled N in Fig. A1, of a larger radio source with $LAS \sim 11$ arcsec ($LS \sim 93$ kpc at $z=2.119$). Both components are elongated at low frequencies. No evidence of the source core is found in our VLA images. The high fractional polarization of component N and the RM consistent with the Galactic value (Table 6) support the idea that the emission is not embedded within the ISM of the host galaxy. Moreover, EVN observations of component N could detect only a set of knots, none reminiscent of the core component (Dallacasa et al. 2002b). On the basis of these new pieces of evidence we classify B3-0754+396 as an LSO, and remove it from the sample of CSS sources.

4.3.7 B3-0810+460B - active

The source has a double structure in our VLA images, while it is resolved into three main components in eMERLIN images. Component S1 might host the source core and its steep spectrum ($\alpha \sim 1.1$) may be due to the combination of core+jet emission which cannot be spatially resolved by our observations. If we compare the eMERLIN flux density at 4.8 GHz with high-resolution VLA data at 15 GHz from Rossetti et al. (2006) we derive a relatively flat spectrum ($\alpha_{4.8}^{15} \sim 0.5$) supporting its interpretation as the source core. EVN observations at 18 cm could detect only components N and S1, while component S2 is completely resolved out, indicating its extended structure (Dallacasa et al. 2002b). No significant flux density asymmetry is observed between the northern and southern (S1+S2) components (Tables 3 and 5, and Rossetti et al. (2006)). The source is slightly polarized in S band. The CI model provides a good fit to the radio spectrum, supporting the active nature of the source.

4.3.8 B3-0856+406 - restarted?

The source has a double structure in our VLA images, while it is resolved into three main components in eMERLIN images. The component labelled C in Fig. A3 is likely the source core. Components E and W have a relatively steep spectrum both in our eMERLIN observations and in VLA data. Component E is the brightest one with a flux density ratio ranging between 3.3, in eMERLIN data at 1.4 GHz, and 1.1 in our VLA data at 14 GHz. In high-resolution VLA

data at 15 GHz, only component E was detected, indicating that component W has a steep spectrum and is likely extended (Rossetti et al. 2006). Although component E is compact in high-resolution 15-GHz images, its spectrum is steep ($\alpha > 1.3$) both in our VLA and eMERLIN data. Neither component C was picked up in that dataset. The source is unpolarized in our images in L and S bands. Both CI and CI OFF models provide a similar fit to the spectrum (though with a rather large value of the reduced chi-square), with the latter slightly preferred over the former. This source is the only one together with the relic B3-0003+387 (out of the 42 analysed) whose spectrum was significantly better fitted with a JP model rather than a CI one in Rossetti et al. (2006). These pieces of evidence suggest that the radio emission of this source has restarted not long ago. However, owing to the presence of a compact region in component E, though with a steep spectrum, we conservatively classify this object as a candidate restarted.

4.3.9 B3-1016+443 - remnant

The source has a double structure in our VLBA image at 4.8 GHz (Fig. A2) and at 1.7 GHz (Dallacasa et al. 2002a). At 8.4 GHz only the northern component is detected. The spectrum of both components is steep and there is no evidence of the source core. Both SSA+CI and SSA+CI OFF models provide a similar fit to the spectrum, with the former slightly preferred over the latter. However, the few data points available leave large uncertainties on the fit results and more data points are needed for a proper model of the synchrotron spectrum. Our classification of B3-1016+443 as a remnant is based on the multi-frequency morphology and spectral index information.

4.3.10 B3-1039+424 - LSO

The source that was classified as a CSS in Fanti et al. (2001) turns out to be the southern lobe/hotspot, labelled S in Fig. A1, of a larger radio source with $LAS \sim 19$ arcsec ($LS \sim 154$ kpc assuming $z=1.05$). The faint core is roughly midway between the northern and southern components. The RM of component S is consistent with the Galactic value (Table 6) suggesting that the radio emission is not embedded within the ISM of the host galaxy. On the basis of these new pieces of evidence we classify B3-1039+424 as an LSO, and remove it from the sample of CSS sources.

4.3.11 B3-1049+384 - active

The source is characterized by 4 components with an unusual morphology. Components W1 and W2 seem a scaled-down version of a double radio galaxy, and their elongation is misaligned with respect to components E and C. Component C has a flat spectrum and is likely the source core. A high flux density asymmetry is observed between the eastern and western (W1+W2) components (Table 4). The SSA+CI model provides a good fit to the radio spectrum, supporting the active nature of the source.

4.3.12 B3-1133+432 - active?

This source is a CSO with a double structure and no evidence of the source core. VLBA images were presented in [Dallacasa et al. \(2002a\)](#) and [Orienti et al. \(2004\)](#). The northern component is the brightest, with a flux density that is roughly double that of the southern component. The spectral index is $\alpha_{1.7}^{4.8} \sim 0.9$ and 1.0 for component N and S, respectively, and slightly steepens between 4.8 and 8.4 GHz ($\alpha_{4.8}^{8.4} \sim 1.2$, [Orienti et al. 2004](#)). The SSA+CI model provides a better fit than the SSA+CI OFF model. However, the few data points available leave large uncertainties on the fit results. Although the core is not detected, we conservatively consider B3+1133+432 as a candidate active source.

4.3.13 B3-1143+456 - active?

This source has a double structure in VLA and eMERLIN images. Both components have a steep spectrum and there is no evidence of the source core. However, if we compare the eMERLIN flux density at 4.8 GHz with high-resolution VLA data at 15 GHz from [Rossetti et al. \(2006\)](#) we derive $\alpha_{4.8}^{15} \sim 0.5$ and 0.7 for component N and S, respectively, suggesting that they may be active hotspots. However, we notice that these are not compact regions, and the spectral index may be artificially flat, due to missing flux density from extended structures unrecovered by eMERLIN observations. The flux density ratio between component N and S is about 5-7 depending on the frequency, with the southern being the brightest one. The source is unpolarized in L and S bands. Both SSA+CI and SSA+CI OFF models give a similar fit to the spectrum, with the former providing a slightly lower value of the reduced chi-square value.

4.3.14 B3-1212+380 - active

This source has a double structure in eMERLIN images and in the high-resolution 15-GHz VLA image ([Rossetti et al. 2006](#)), while in our VLA observations the source is unresolved in L and S bands, and slightly resolved in U band. In eMERLIN images the southern component is slightly resolved into two components elongated in the NW-SE direction. Component S1 might host the source core, and the steep spectrum of the whole southern component may arise from the blending of the core emission with that of the steep-spectrum jet and mini-lobe. This interpretation is supported by the estimate of the spectral index of S1 between eMERLIN data at 4.8 GHz and high-resolution VLA data at 15 GHz ([Rossetti et al. 2006](#)), which turns out to be $\alpha_{4.8}^{15} \sim 0$. The low data quality of EVN observations could not help identify the core component ([Dallacasa et al. 2002b](#)). In eMERLIN images where the source structure is resolved, there is no significant flux density asymmetry between the northern and southern components (Table 5). The source is unpolarized in our images in L and S bands. The CI model provides a good fit to the radio spectrum, supporting the active nature of the source.

4.3.15 B3-1216+402 - remnant?

This source has a double structure in our VLA images. There is no evidence of the source core. The spectral index $\alpha \sim 1.0$, i.e. not ultra-steep as it is found in other sources, may indicate the co-existence of aged emission from lobes with the contribution of active regions like hotspots, which are mixed up with the resolution of our observations. However, in high resolution 15-GHz VLA observations only the southern component hosts a faint steep-spectrum compact region, while the structure of the northern component is fragmented, with no clear indication of a hotspot. Neither the core is detected in this data set ([Rossetti et al. 2006](#)). There is no significant flux density asymmetry between the northern and southern components at low frequencies, while it becomes roughly double at 14 GHz, with the southern being the brightest (Table 3). Polarization increases from L to S band, and is detected in both components, with component N significantly polarized in S band (8.5 per cent). Both CI and CI OFF models provide a similar fit to the spectrum. The lack of a clear core detection and the possible presence of a candidate hotspot, (though with a relatively steep spectrum) in the southern component make us conservatively classify this object as a candidate remnant.

4.3.16 B3-1225+442 - restarted

Although at 1.7 GHz the source shows a triple morphology ([Dallacasa et al. 2002a](#)), at 8.4 GHz it has a double structure, being the westernmost component, labelled W2 in [Dallacasa et al. \(2002a\)](#) undetected at high frequency. Only the central component, labelled W1 in [Dallacasa et al. \(2002a\)](#), and the eastern one are detected in our observations. The component labelled E in Fig. A2 is severely resolved out, whereas the other component is resolved into two sub-components labelled W1A and W1B. The spectral index of W1A is flat ($\alpha \sim 0.1$) indicating that the source core may be hosted in this component. The lack of compact components at the edge of the source and the possible presence of the core may indicate that the radio emission has restarted not long ago. The SSA+CI OFF model provides a slightly better fit than the SSA+CI model, supporting the recent restart of the radio emission.

4.3.17 B3-1340+439 - restarted?

The source is resolved into several sub-components in our VLBA images. The component labelled C in Fig. A2 has a rather flat spectrum and is likely the source core. Component S is severely resolved out at 8.3 GHz, while component N1, though with a rather compact structure at 8.3 GHz, has a steep spectrum ($\alpha_{4.8}^{8.3} \sim 1.9$). The northern component (N1+N2+N3) is brighter than the southern one, with a flux density ratio >10 . The SSA+CI OFF model provides a slightly better fit than the SSA+CI one. As in the case of B3-0856+406 and B3-1225+442, these pieces of evidence may indicate that the radio emission in this source has restarted not long ago. However, the morphology of the northern components is consistent with a jet structure, making us conservatively consider this source as a candidate

restarted.

4.3.18 B3-1449+421 - active

The source is resolved into several sub-components in our VLBA images. The component labelled C in Fig. A2 is likely the source core, and the rather steep spectrum may be due to the combination of core+jet emission that cannot be resolved by our observations. The morphology of the southern components is consistent with a jet structure. There is no significant flux density ratio (~ 1) between the northern and southern components. The SSA+CI model provides a good fit to the radio spectrum, supporting the active nature of the source.

5 DISCUSSION

A possible explanation for the high number of intrinsically compact extragalactic radio sources is the intermittency of short-lived episodes of jet activity. Several models predict that the dominant population of extragalactic radio sources consists in short-lived objects (e.g. Reynolds & Begelman 1997; Hardcastle 2018; Shabala et al. 2020) which may not evolve into classical Fanaroff-Riley type I/II radio galaxies. The straightforward outcome from this scenario is the existence of a population of young but dying radio sources. To unveil the incidence of remnants in the population of young radio sources we study the statistically complete B3-VLA CSS sample and we searched for active regions in the 18 sources with a steep ($\alpha_{4.8}^{8.4} > 1.0$) integrated radio spectrum and without any evidence of the core from earlier observations. These could be considered the signatures of an aged population of relativistic electrons, without a significant contribution from freshly produced/accelerated ones.

The wide frequency coverage and the deep sensitivity of our new observations allowed us to classify the sources in either active or remnants. We find that 3 CSS sources selected by Fanti et al. (2001) are components of large radio sources, and we remove them from the CSS sample. The final sample thus consists of 84 objects divided into 25 sources with $LAS < 0.25$ arcsec, that we consider as CSOs (though the core is not detected in all of them), while 59 sources have $LAS > 0.25$ arcsec, that we classify as MSOs.

5.1 Core detection

We detect the core component in 10 sources of our sample (inclusive of LSOs), while in 6 CSS sources we could set an upper limit on its flux density. The radio morphology of B3-0034+444 precludes us from determining the location of the core or setting a tight upper limit.

In Fig. 2 we plot the ratio between the core luminosity P_c at 5 GHz vs the total source luminosity P_{tot} at 408 MHz for the sources of the B3-VLA CSS sample, with the exception of the three LSOs (all luminosities are k-corrected).

Table 7. Summary of core detection and candidate remnants/restarted sources. Column 1: class of objects; column 2: number of sources in the B3-VLA CSS sample; column 3: number of sources of the sample studied in this work; column 4: number of core detected in the data presented here (total number of core detected for the whole B3-VLA CSS sample including information from the literature); column 5: number of (candidate) remnants/restarted sources.

Class	B3-VLA CSS	this sample	core	remnants/ restarted
All CSS	84	15	8 (44)	3/3
CSOs	25	6	4 (12)	1/2
MSOs	59	9	4 (30)	2/1
LSOs	3	3	2 (2)	-

When no information at 5 GHz is available for the core component, we extrapolate the flux density assuming a flat spectral index $\alpha = 0$. If the core is undetected at all frequencies we assume as upper limit the three sigma noise level of either the high-resolution VLA images at 15 GHz reported in Rossetti et al. (2006) for MSOs, or the VLBA images at 8.4 GHz for CSOs⁴. When the redshift is unknown, we assume $z = 1.05$ (see Fanti et al. 2001).

In Fig. 2 we plot the best fit (corrected for the cosmology adopted in this paper) that is obtained for the 3CR radio galaxies (Giovannini et al. 1988), i.e. for objects with a luminosity between 10^{24-28} W Hz⁻¹. CSS sources from the B3-VLA are in general above the best fit. If we perform a regression fit that minimizes the chi-square error statistics, we obtain for the CSS sources:

$$\text{Log } P_c = (8.0 \pm 5.3) - (0.6 \pm 0.2) \times \text{log } P_{tot} .$$

This empirical relation has a slope (though with large uncertainty) that is similar to the one found by Giovannini et al. (1988), but it is slightly shifted towards higher luminosities. This may be due to the slightly higher luminosities of the B3-VLA CSS sample, i.e. about $10^{26} - 10^{29}$ W Hz⁻¹ (Fanti et al. 2001).

For the CSS sources with no detection of the core component we could set a tight upper limit on the luminosity, with the exception of B3-0034+444, which is in general well below the average trends, suggesting that some might be remnants. However, we cannot exclude the possibility that some level of core activity (below the sensitivity threshold) is present. A very weak core and the steep spectrum of the source may indicate that either some level of activity of the AGN is always present, even if it is unable to launch powerful jets, or that the radio core has just switched on again (Jurlin et al. 2021). Apart from a few objects where the optical counter-

⁴ We do not consider all the sources from the B3-VLA CSS sample without the core detection, but only those showing a morphology, mainly a double structure, for which it is reasonable to set an upper limit to the flux density related to the rms of the images. For those sources with a complex morphology, the core may be hidden by other components, like jets and low-surface brightness emission from lobes that bridges the outermost hotspot regions (e.g. B3-0902+416).

part is unknown, all the sources of our sample are optically classified as galaxies rather than quasars (i.e. jets oriented at a large angle with respect to our line of sight). Therefore, we cannot exclude the possibility that the core flux density may be Doppler diminished and thus non-detected by our observations due to sensitivity limitation (see e.g., Saikia & Kulkarni 1994).

5.2 Remnants and restarted sources

The analysis of the integrated radio spectrum points out that 5 sources are best fitted by a continuous particle injection model, while other 5 sources require the inclusion of a relic phase. For the remaining 5 CSS sources both models provide a quite equivalent good fit to their spectra (CI OFF model approaches CI model).

For LSOs are contaminant of our sample, they are dropped from our analysis since they do not belong to the sample of subgalactic size radio sources.

To unveil whether a source is active or not, we need to correctly determine both the integrated synchrotron spectrum, and the nature of each sub-structure: extended vs compact regions, and spectral index information. For the sources of our sample we find that 9 are likely active: 5 with a secure classification, and 4 candidate active objects. The latter are radio sources with no core detection, but with the presence of a hotspot (with $\alpha < 0.7$ at least on one side). The non detection of a hotspot on both sides of the radio emission may be an indication of an inhomogeneous environment. 11 out of the 15 MSOs/CSOs sources of our sample show significant flux density asymmetry (i.e. flux density ratio $\gg 1$) between the two sides of the radio emission, whereas polarization asymmetry is observed in 4 of the sources with polarization information. Asymmetries in flux density, polarization, and arm-length ratio between the two sides of the radio emission caused by an inhomogeneous medium have been found more often in young radio sources than in classical double radio galaxies (see e.g., Saikia & Gupta 2003; Saikia et al. 2003; Orienti & Dallacasa 2008; Dallacasa et al. 2013; Orienti & Dallacasa 2014; Orienti 2016; O’Dea & Saikia 2021).

Among sources with core detection, B3-1225+442 (CSO) is likely a restarted object. Its extended components that are well imaged at low frequency (Dallacasa et al. 2002a) are either undetected or highly resolved-out at the highest frequency, and show a steep spectrum, indicating that no compact active regions, like hotspots, are present at the edges of the sources. On the contrary the central component has a spectral index that is consistent with current activity. The other two sources, B3-0856+406 (MSO) and B3-1340+439 (CSO) are candidate restarted. Their integrated radio spectra are better modelled when a relic period is included, suggesting that the activity has not been continuous during the total source age. However, the presence of an edge-brightened component in B3-0856+406 and a jet-like structure in B3-1340+439 make us conservatively consider these objects candidate restarted.

We classify the remaining sources B3-0003+387 (MSO) and B3-1016+443 (CSO) as remnants, while we conservatively consider B3-1216+482 (MSO) a candidate remnant.

The improvement in sensitivity and angular resolution

that will be achieved with the next generation of radio facilities, like the Square Kilometre Array (SKA) and the next-generation VLA (ngVLA), will allow us to study the radio spectra of each component of the radio sources (i.e. similar to the spectral studies currently done for radio galaxies with sizes of hundred of kpc and beyond), rather than the integrated one, providing a robust classification of the activity of young radio sources.

Detecting young radio sources already in a remnant/restarted phase strongly supports the power-law distribution of the source ages (e.g. Hardcastle 2018; Shabala et al. 2020; Morganti et al. 2021) implying that not all the radio sources will evolve into large and old radio galaxies. The detection of only three possible cases of restarted sources suggests that the remnant phase in young objects is shorter than the time elapsed between the end of the first epoch and the start of the second epoch of activity (i.e. 10^{3-5} yr). In CSS sources the decay of the radio emission may be faster than in larger sources due to the magnetic field (about a few mG, Fanti et al. 1995; Dallacasa et al. 2002a; Orienti et al. 2004; Orienti & Dallacasa 2008) that is usually orders of magnitude higher than in extended radio galaxies (about a few μ G, Croston et al. 2005; Brienza et al. 2016; Ineson et al. 2017). On the other hand, inverse-Compton losses should not play a major role since the equivalent magnetic field of the cosmic microwave background for the source at the highest redshift is about 50 μ G, i.e. much lower than the magnetic field of the radio source. Similarly, inverse Compton losses due to the upscattering of various surrounding photon fields (disc, torus, stars) by the lobes’ electrons should be negligible (Stawarz et al. 2008).

For the sources of the B3-VLA CSS sample span a large redshift range, the steepness of the spectrum may be due to the z - α correlation (e.g., Ker et al. 2012; Morabito & Harwood 2018), rather than the ageing. In Fig. 3 we plot the α - z correlation for the sources of our sample divided into active (open stars) and (candidate) remnant/restarted (filled stars), together with the radio sources from the whole B3-VLA CSS (open circles). Only radio sources with a spectroscopic redshift have been considered since we notice some discrepancy between photometric and spectroscopic redshifts that may affect the results of the correlation. The majority of the sources from our sample are indistinguishable from those of the B3-VLA CSS, suggesting that the redshift should not act as a main character in the steepness of the spectrum. B3-0856+406 seems an outlier, with its steep spectrum likely due to a combination of both high redshift and ageing of the radio emission.

We remark that among the sources of the B3-VLA CSS sample not observed here, there are other objects lacking a secure core detection and showing radio structures dominated by extended low-surface brightness features. Although their integrated spectrum is not ultra-steep, we cannot exclude that there may be some sources that have either switched off recently, or their radio emission has just restarted. For this reason the percentages from this work should be considered lower limits. Multi-frequency high angular resolution observations of these remaining sources are thus crucial for unveiling the incidence of restarted/remnants objects among the population of CSS

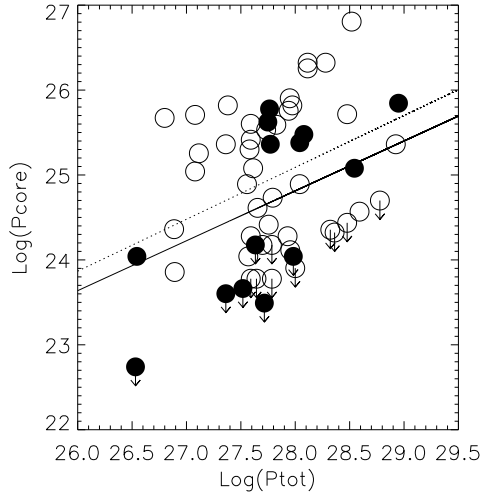


Figure 2. Core luminosity at 5 GHz vs total luminosity at 408 MHz of the sources from the B3-VLA CSS sample (see Section 5.1). Empty circles are CSS sources from the B3-VLA CSS sample (Fanti et al. 2001), while filled circles are the sources studied in this paper (with the exception of B3-0034+444 and LSOs). The solid line represents the relation obtained for 3CR radio sources (Giovannini et al. 1988) corrected for the cosmology adopted in this paper, while the dotted line represents the best fit for CSS sources from the B3-VLA CSS sample (see Section 5.1.) Downward arrows indicate upper limits.

sources.

6 SUMMARY

This paper presents the first study of the incidence of remnant/restarted radio sources in a complete sample of CSS objects, making use of multi-frequency VLA, pc-scale VLBA, and eMERLIN observations of 18 candidate remnants from the B3-VLA CSS complete sample. The conclusions that we can draw from this investigation are:

- we detect the core region in 10 radio sources;
- we find that 3 sources (2 MSOs and 1 CSO) out of the 18 studied in this paper are likely remnants: two with a rather secure classification, while the remaining one is conservatively classified as a candidate remnant;
- among the sources with core detection, two CSOs and 1 MSO are likely restarted radio sources (one with a rather robust classification, while two conservatively considered candidates). These sources, together with B3-0003+387 and B3-0128+394, are the only five objects whose synchrotron spectra are better reproduced by a CI+OFF model than a CI one;
- we discovered that 3 objects are not CSS sources but components of larger radio sources, and we remove them from the B3-VLA CSS sample;
- significant flux density asymmetry is observed in 11 out of 15 MSOs/CSOs of our sample, in agreement with the high fraction of asymmetric objects found in other samples of compact and young radio sources.

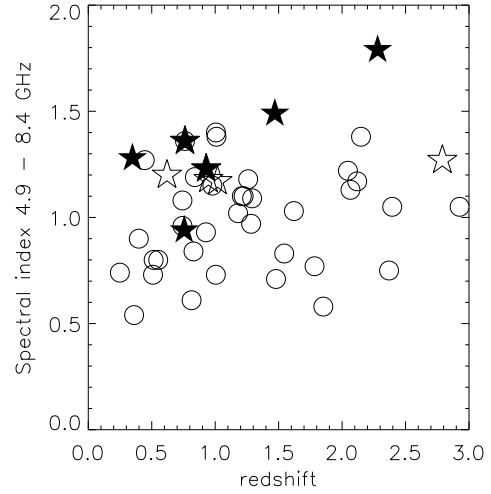


Figure 3. Observed-frame spectral index between 4.9 and 8.4 GHz vs redshift of the sources from our sample either (candidate-)remnant/restarted (filled stars) or (candidate-)active (open stars) together with the remaining sources of the B3-VLA CSS. Only sources with spectroscopic redshift have been considered.

In order to extend the percentage of remnants and restarted sources to the whole B3-VLA CSS sample we need further high-resolution observations of those sources still lacking multi-frequency data.

Determining the incidence of young but fading radio sources that can be observed by current and future facilities is paramount. A complete characterization of the life-cycle of the radio emission from relativistic jets will be fundamental for the exploitation of the data from the forthcoming facilities, like SKA and ngVLA. Thanks to the significant improvement in sensitivity and resolution, SKA and ngVLA will allow systematic studies of populations of fainter and farther radio sources, providing a fundamental step forward in our understanding of their cosmological evolution.

ACKNOWLEDGMENTS

We thank the referee, D. Saikia, for reading the manuscript carefully and making valuable suggestions. The VLA and VLBA are operated by the US National Radio Astronomy Observatory which is a facility of the National Science Foundation operated under cooperative agreement by Associated Universities, Inc. e-MERLIN is a National Facility operated by the University of Manchester at Jodrell Bank Observatory on behalf of STFC, part of UK Research and Innovation. This work has made use of the NASA/IPAC Extragalactic Database NED which is operated by the JPL, Californian Institute of Technology, under contract with the National Aeronautics and Space Administration. AIPS is produced and maintained by the National Radio Astronomy Observatory, a facility of the National Science Foundation operated under cooperative agreement by Associated Universities, Inc. Funding for the Sloan

Digital Sky Survey IV has been provided by the Alfred P. Sloan Foundation, the U.S. Department of Energy Office of Science, and the Participating Institutions. SDSS acknowledges support and resources from the Center for High-Performance Computing at the University of Utah. The SDSS web site is www.sdss.org. SDSS is managed by the Astrophysical Research Consortium for the Participating Institutions of the SDSS Collaboration including the Brazilian Participation Group, the Carnegie Institution for Science, Carnegie Mellon University, Center for Astrophysics | Harvard & Smithsonian (CfA), the Chilean Participation Group, the French Participation Group, Instituto de Astrofísica de Canarias, The Johns Hopkins University, Kavli Institute for the Physics and Mathematics of the Universe (IPMU) / University of Tokyo, the Korean Participation Group, Lawrence Berkeley National Laboratory, Leibniz Institut für Astrophysik Potsdam (AIP), Max-Planck-Institut für Astronomie (MPIA Heidelberg), Max-Planck-Institut für Astrophysik (MPA Garching), Max-Planck-Institut für Extraterrestrische Physik (MPE), National Astronomical Observatories of China, New Mexico State University, New York University, University of Notre Dame, Observatório Nacional / MCTI, The Ohio State University, Pennsylvania State University, Shanghai Astronomical Observatory, United Kingdom Participation Group, Universidad Nacional Autónoma de México, University of Arizona, University of Colorado Boulder, University of Oxford, University of Portsmouth, University of Utah, University of Virginia, University of Washington, University of Wisconsin, Vanderbilt University, and Yale University.

DATA AVAILABILITY

The data underlying this article are available in the NRAO Data Archive (<https://science.nrao.edu/observing/data-archive>) with the project codes BO038, 15A-140, 16B-107, and 17B-153. Calibrated data are available upon reasonable request.

REFERENCES

- Albareti, F., et al. 2017, *ApJS*, 233, 25
- Allington-Smith, J.R., Spinrad, H., Djorgovski, S., Liebert, J. 1988, *MNRAS*, 234, 1091
- Brienza, M., et al. 2016, *A&A*, 585, 29
- Brienza, M., et al. 2017, *A&A*, 606, 98
- Brocksopp, C., Kaiser, C.R., Schoenmakers, A.P., de Bruyn, A.G. 2007, *MNRAS*, 382, 1019
- Callingham, J.R. 2015, *ApJ*, 809, 168
- Cohen, A.S., Lane, W.M., Cotton, W.D., Kassim, N.E., Lazio, T.J.W., Perley, R.A., Condon, J.J., Erickson, W.C. 2007, *AJ*, 134, 1245
- Croston, J.H., Hardcastle, M.J., Harris, D.E., Belsole, E., Birkinshaw, M., Worrall, D.M. 2005, *ApJ*, 626, 733
- Cruz, M.J., et al. 2006, *MNRAS*, 373, 1531
- Czerny, B., Siemiginowska, A., Janiuk, A., Nikiel-Wroczyński, B., Stawarz, L. 2009, *ApJ*, 698, 840
- Dallacasa, D., Tinti, S., Fanti, C., Fanti, R., Gregorini, L., Stanghellini, C., Vigotti, M. 2002a, *A&A*, 389, 115
- Dallacasa, D., Fanti, C., Giacintucci, S., Stanghellini, C., Fanti, R., Gregorini, L., Vigotti, M. 2002b, *A&A*, 389, 126
- Dallacasa, D., Orienti, M., Fanti, C., Fanti, R., Stanghellini, C. 2013, *MNRAS*, 433, 147
- Fanti, C., Fanti, R., Dallacasa, D., Schilizzi, R.T., Spencer, R.E., Stanghellini, C. 1995, *A&A*, 302, 31
- Fanti, C., Pozzi, F., Dallacasa, D., Fanti, R., Gregorini, L., Stanghellini, C., Vigotti, M. 2001, *A&A*, 369, 380
- Fanti, C., Fanti, R., Zanichelli, A., Dallacasa, D., Stanghellini, C. 2011, *A&A*, 528, 110
- Ficarra, A., Grueff, G., Tomassetti, G. 1985, *A&AS*, 59, 25
- Giovannini, G., Feretti, L., Gregorini, L., Parma, P. 1988, *A&A*, 199, 73
- Godfrey, L.E.H., Morganti, M., Brienza, M. 2017, *MNRAS*, 471, 891
- Gugliucci, N.E., Taylor, G.B., Peck, A.B., Giroletti, M. 2005, *ApJ*, 622, 136
- Hardcastle, M.J., et al. 2016, *MNRAS*, 462, 1910
- Hardcastle, M.J., et al. 2018, *MNRAS*, 475, 2768
- Hardcastle, M.J., et al. 2019, *A&A*, 622, 12
- Harwood, J.J., et al. 2017, *MNRAS*, 638, 34
- Hota, A., et al. 2011, *MNRAS*, 417, 36
- Ineson, J., Croston, J.H., Hardcastle, M.J., Mingo, B. 2017, *MNRAS*, 467, 1587
- Intema, H.T., Jagannathan, P., Mooley, K.P., Frail, D.A. 2017, *A&A*, 598, 78
- Jaffe, W.J., Perola, G.C. 1973, *A&A*, 26, 423
- Jarvis, M.J., et al. 2001, *MNRAS*, 326, 1563
- Jurlin, N., et al. 2020, *A&A*, 638, 34
- Jurlin, N., et al. 2021, *A&A*, in press (arXiv:2106.13161)
- Kardashev, N.S. 1962, *SvA*, 6, 317
- Ker, L.M., Best, P.N., Rigby, E.E., Röttgering, H.J.A., Gendre, M.A. 2012, *MNRAS*, 420, 2644
- Komissarov, S.S., Gubanov, A.G. 1994, *A&A*, 285, 27
- Konar, C., Saikia, D. J., Jamroz, M., Machalski, J. 2006, *MNRAS*, 372, 693
- Kunert-Bajraszewska, M., Marecki, A. 2007, *A&A*, 469, 437
- Lane, W.M., Cotton, W.D., van Velzen, S., Clarke, T.E., Kassim, N.E., Helmboldt, J.F., Lazio, T.J.W., Cohen, A.S. 2014, *MNRAS*, 440, 327
- Lara, L., Márquez, I., Cotton, W.D., Feretti, L., Giovannini, G., Marcaide, J.M., Venturi, T. 1999, *A&A*, 348, 699
- Luo, W.-F., Yang, J., Cui, L., Liu, X., Shen, Z.-Q. 2007, *ChJAA*, 7, 611
- Mahatma, V.H., et al. 2018, *MNRAS*, 475, 4557
- Mahatma, V.H., et al. 2019, *A&A*, 622, 13
- McMullin J. P., Waters B., Schiebel D., Young W., Golap K., 2007, in Shaw R. A., Hill F., Bell D. J., eds., *ASP Conf. Ser. Vol. 376, Astromical Data Analysis and Systems XVI*, Astron. Soc. Pac. San Francisco, p. 127
- Morabito, L.K., Harwood, J.J. 2018, *MNRAS*, 480, 2726
- Morganti, R. 2017, *NatAs*, 1, 596
- Morganti, R., et al. 2021, *A&A*, 648, 9
- Murgia, M., Fanti, C., Fanti, R., Gregorini, L., Klein, U., Mack, K.-H., Vigotti, M. 1999, *A&A*, 345, 769
- Murgia, M. 2003, *PASA*, 20, 19
- Murgia, M., et al. 2011, *A&A*, 526, 148
- Nyland, K., et al. 2020, *ApJ*, 905, 74
- O’Dea, C.P., Saikia, D.J. 2021, *A&ARv*, 29, 3
- Orienti, M., Dallacasa, D., Fanti, C., Fanti, R., Tinti, S., Stanghellini, C. 2004, *A&A*, 426, 463
- Orienti, M., Dallacasa, D. 2008, *A&A*, 487, 885
- Orienti, M., Murgia, M., Dallacasa, D. 2010, *MNRAS*, 402, 1892
- Orienti, M., Dallacasa, D. 2014, *MNRAS*, 438, 463
- Orienti, M. 2016, *AN*, 337, 9
- Orienti, M., Dallacasa, D. 2020, *MNRAS*, 499, 1340
- Orrú, E., Murgia, M., Feretti, L., Govoni, F., Giovannini, G., Lane, W., Kassim, N., Paladino, R. 2010, *A&A*, 515, 50
- O’Sullivan, E., Kunert-Bajraszewska, M., Siemiginowska, A.,

- Burke, D.J., Combes, F., Salomé, P., Giacintucci, S. 2021, *ApJ*, 913, 105
- Pahre, M.A., Djorgovski, S.G 1995, *ApJ*, 449, L1
- Parma, P., Murgia, M., de Ruiter, H.R., Fanti, R., Mack, K.-H., Govoni, F. 2007, *A&A*, 470, 875
- Randriamanakoto, Z., Ishwara-Chandra, C.H., Taylor, A. R. 2020, *MNRAS*, 496, 3381
- Rawlings, S., Eales, S., Lacy, M. 2001, *MNRAS*, 322, 523
- Reynolds, C.S., Begelman, M. C. 1997, *ApJ*, 487, 135
- Rossetti, A., Fanti, C., Fanti, R., Dallacasa, D., Stanghellinni, C. 2006, *A&A*, 449, 49
- Rossetti, A., Dallacasa, D., Fanti, C., Fanti, R., Mack, K.-H. 2008, *A&A*, 487, 865
- Saikia, D.J., Kulkarni, V.K. 1994, *MNRAS*, 270, 897
- Saikia, D.J., Gupta, N. 2003, *A&A*, 405, 499
- Saikia, D.J., Jeyakumar, S., Mantovani, F., Salter, C.J., Spencer, R.E., Thomasson, P., Wiita, P.J. 2003, *PASA*, 20, 50
- Saripalli, L., Subrahmanyam, R., Thorat, K., Ekers, R.D., Hunstead, R.W., Johnston, H.M., Sadler, E.M. 2012, *ApJS*, 199, 27
- Schoenmakers, A.P., de Bruyn, A.G., Röttgering, H.J.A., van der Laan, H., Kaiser, C.R. 2000, *MNRAS*, 315, 371
- Shabala, S.S., Jurlin, N., Morganti, R., Brienza, M., Hardcastle, M.J., Godfrey, L.E.H., Krause, M.G.H., Turner, R.J. 2020, *A&A*, 496, 1706
- Singh, V., Ishwara-Chandra, C.H., Kharb, P., Srivastava, S., Jannardhan, P. 2016, *ApJ*, 826, 132
- Slee, O.B., Roy, A.L., Murgia, M., Andernach, H., Ehle, M. 2001, *AJ*, 122, 1172
- Stanghellini, C., O’Dea, C.P., Dallacasa, D., Cassaro, P., Baum, S.A., Fanti, R., Fanti, C. 2005, *A&A*, 443, 891
- Stawarz, L., Ostorero, L., Begelman, M.C., Moderski, R., Kataoka, J., Wagner, S. 2008, *ApJ*, 680, 911
- Taylor, A.R., Stil, J.M., Sunstrum, C. 2009, *ApJ*, 702, 1230
- Thompson, D., Djorgovski, S., Vigotti, M., Grueff, G. 1994, *AJ*, 108, 828
- Thompson, D., Aftreth, O., Soifer, B.T. 2000, *AJ*, 120, 2331
- Tinti, S., Dallacasa, D., de Zotti, G., Celotti, A., Stanghellini, C. 2005, *A&A*, 432, 31
- Wegner, G., Salzer, J.J., Jangren, A., Gronwall, C., Melbourne, J. 2003, *AJ*, 125, 2373

APPENDIX A: IMAGES OF THE TARGET SOURCES

In Figs. A1, A2, and A3 we show images of the sources observed with the VLA, VLBA, and eMERLIN, respectively. On each image, we provide the source name, the observing band, the peak brightness (peak) and the first contour (f.c.), which is three times the off-source noise level on the image plane. Contours increase by a factor of 2. The beam is plotted in the bottom left-hand corner of each image. For the VLA data sets with polarization information, the color-scale represents the polarization intensity, while vectors represent the EVPA.

APPENDIX B: FIELD SOURCES

In L band we had to image several objects that fall within the primary beam of the array. For no high-angular resolution observations are available in the literature, here we provide information on the radio structure and flux density at 1.5 GHz based on images with a resolution of about 1 - 1.5 arcsec (Table B1). Flux density is measured on images

corrected for the response of the primary beam. Images are presented in Fig. B1.

APPENDIX C: SPECTRAL FITS

In Fig. C1 we present the integrated spectrum of the sources along with the best-fit CI model and best-fit CI OFF model. In Table C1 we report the parameters of the fits.

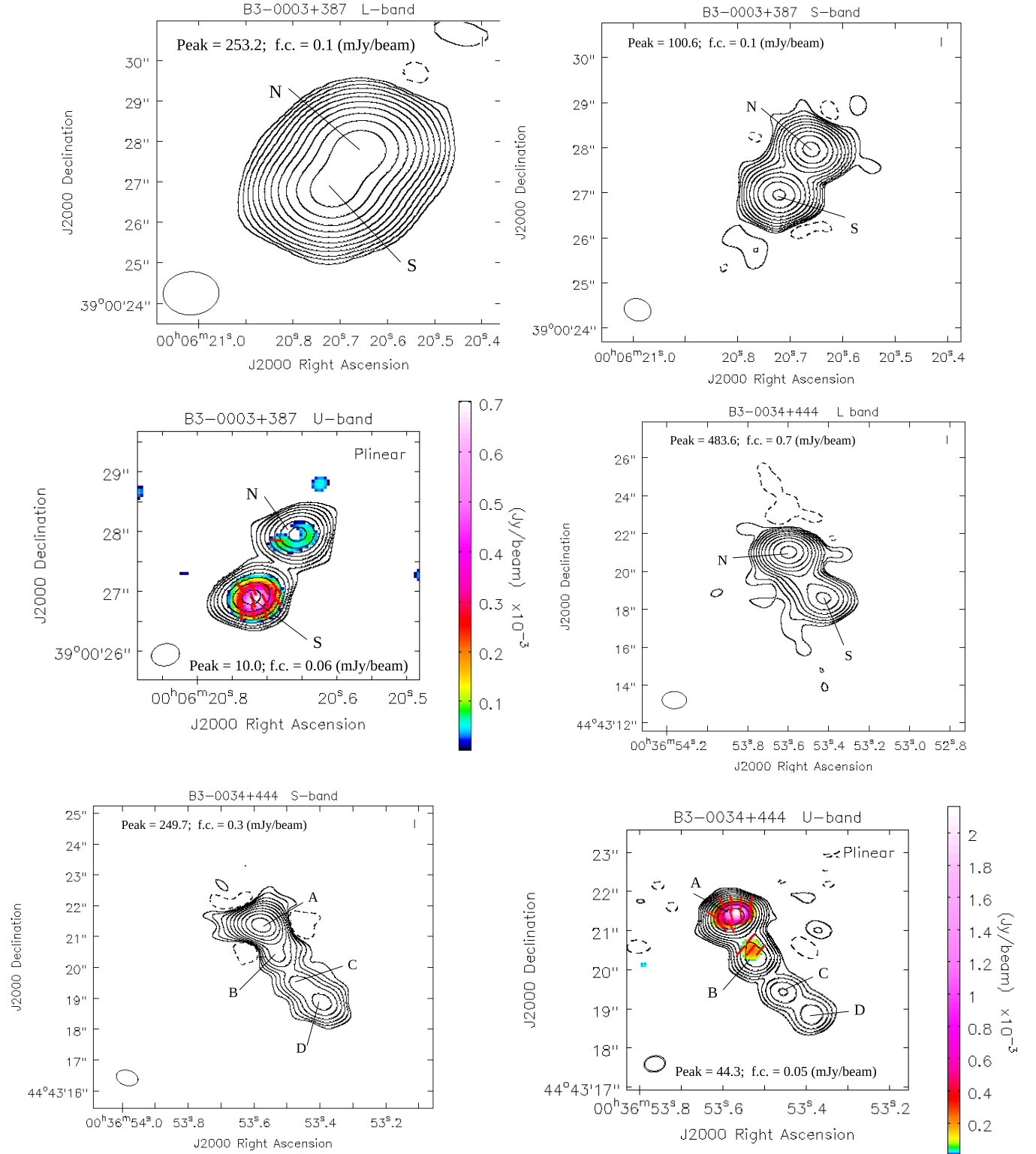


Figure A1. VLA images in L, S and U bands of the CSS sources with LAS > 1 arcsec. On each image, we provide the source name, the observing band, the peak brightness (peak) and the first contour (f.c.), which is three times the off-source noise level on the image plane. Contours increase by a factor of 2. The beam is plotted in the bottom left-hand corner of each image. For the data sets with polarization information, the color-scale represents the polarization intensity, while vectors represent the EVPA.

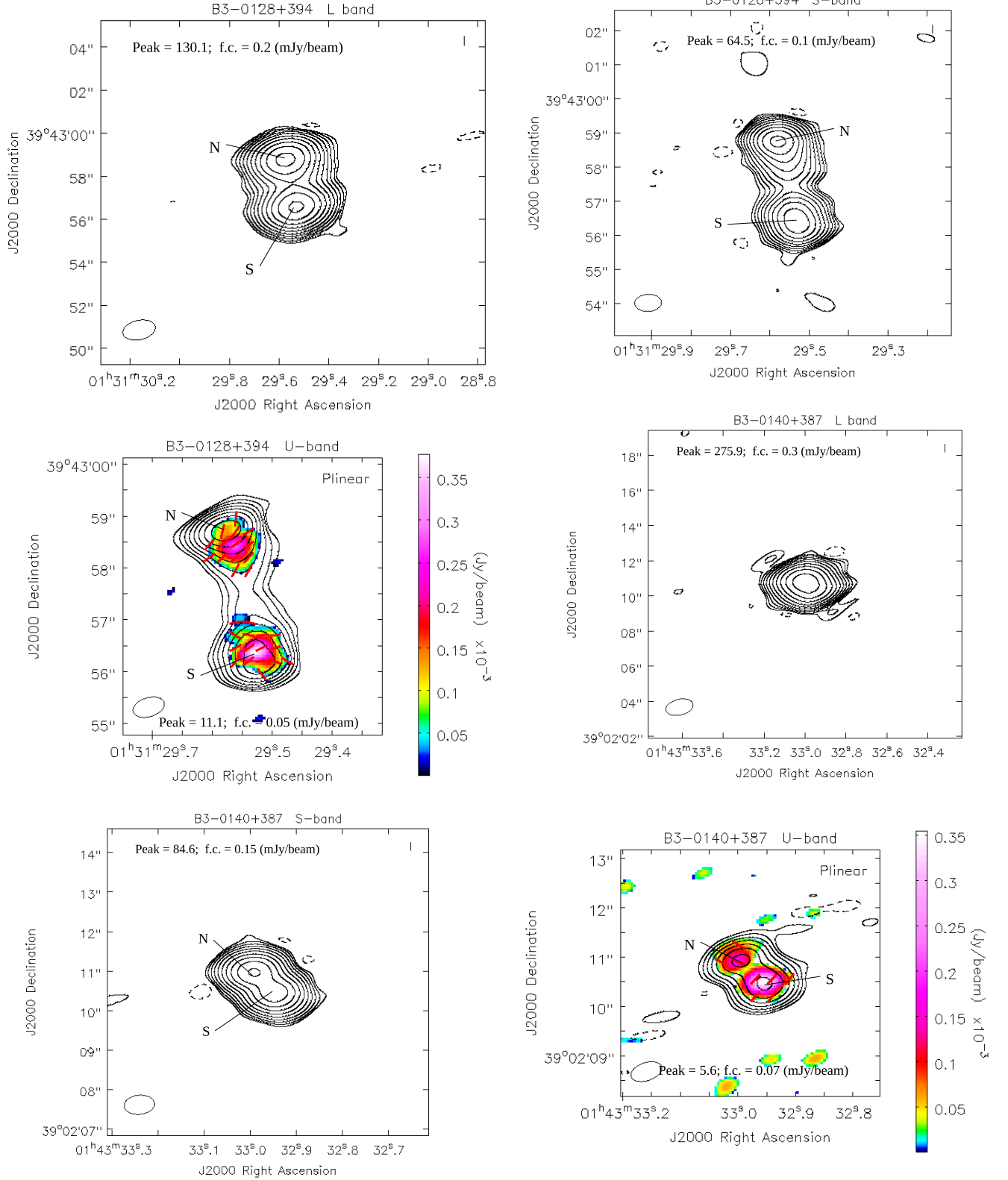


Figure A1. Continued.

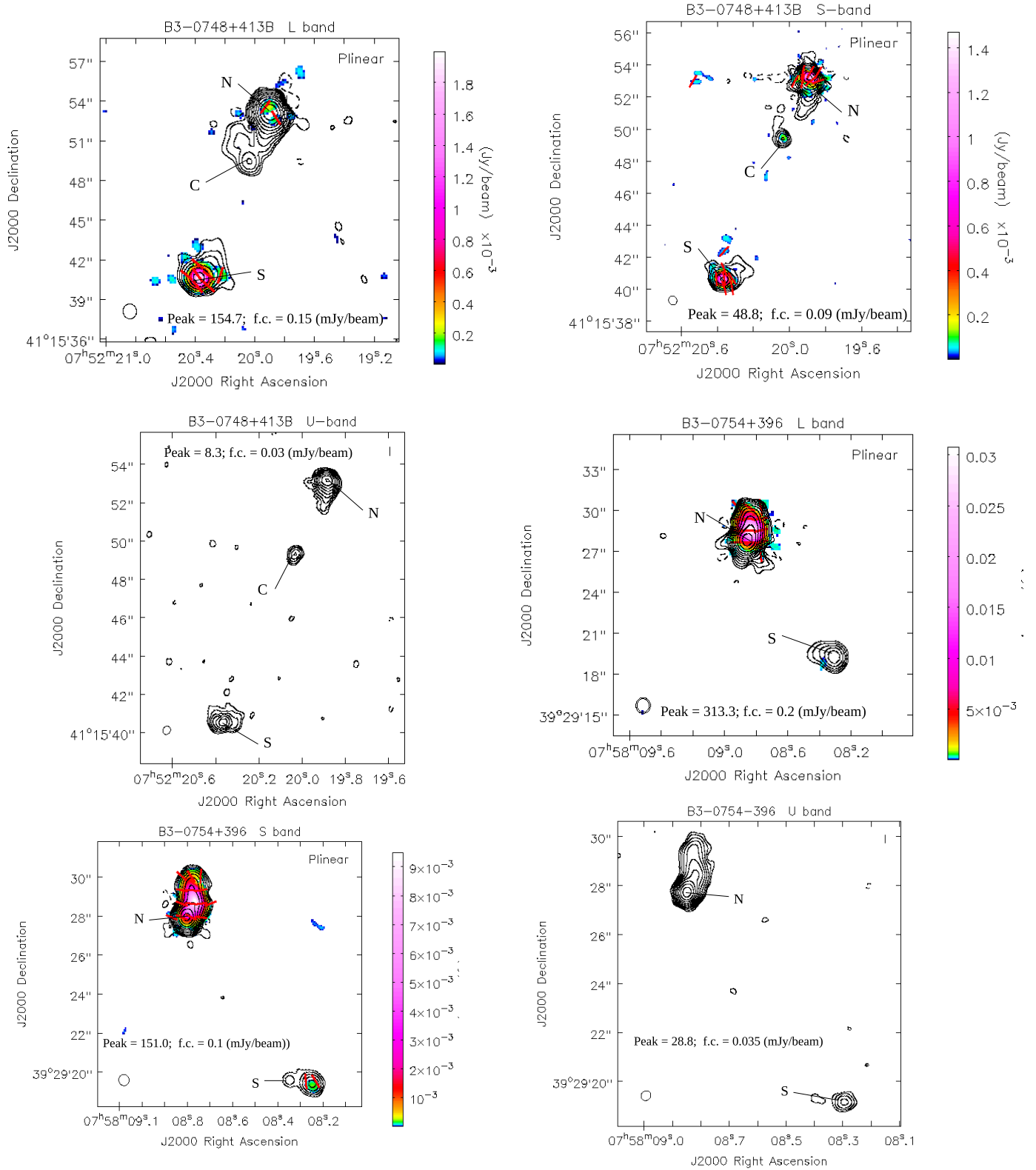


Figure A1. Continued.

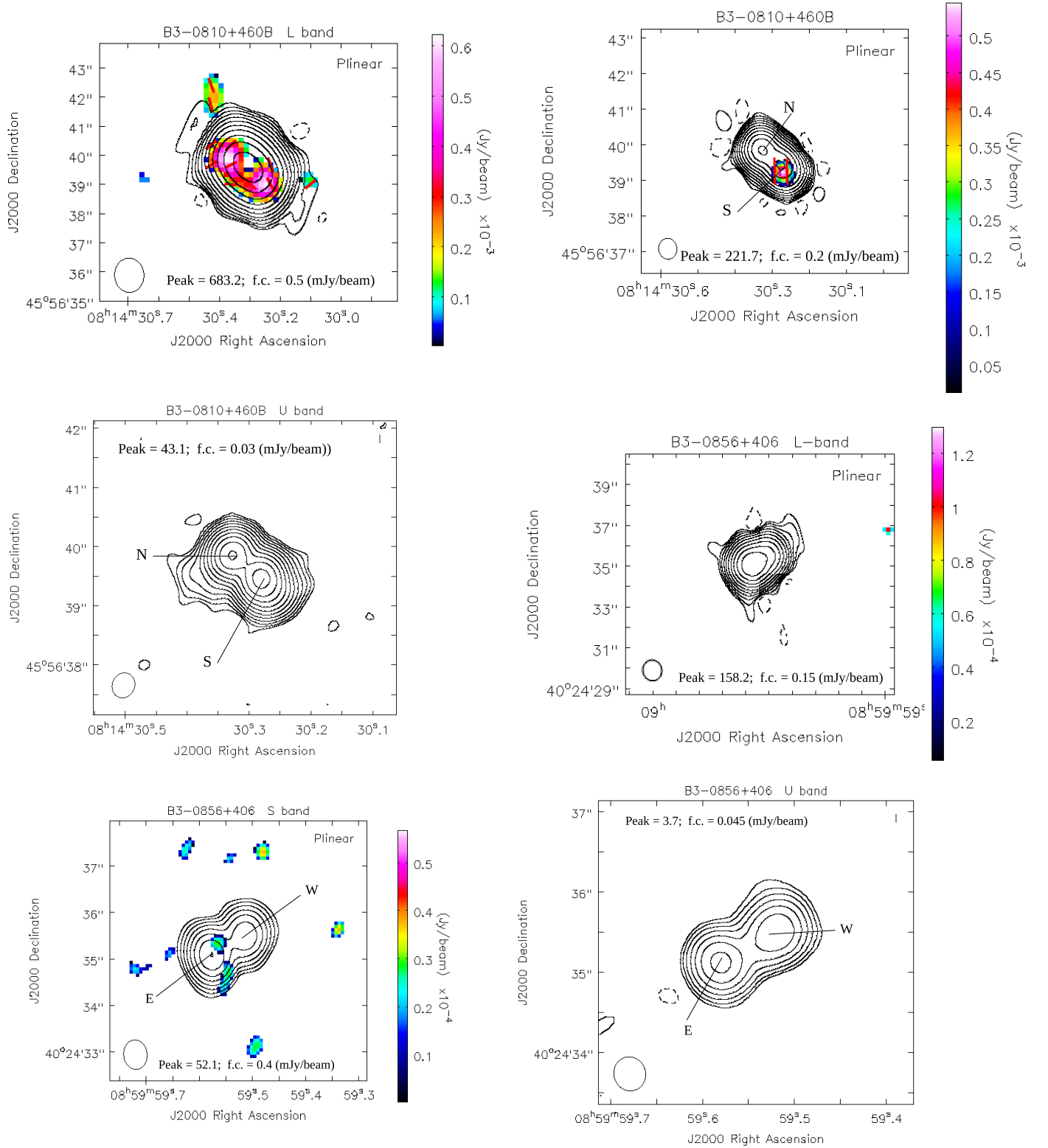


Figure A1. Continued.

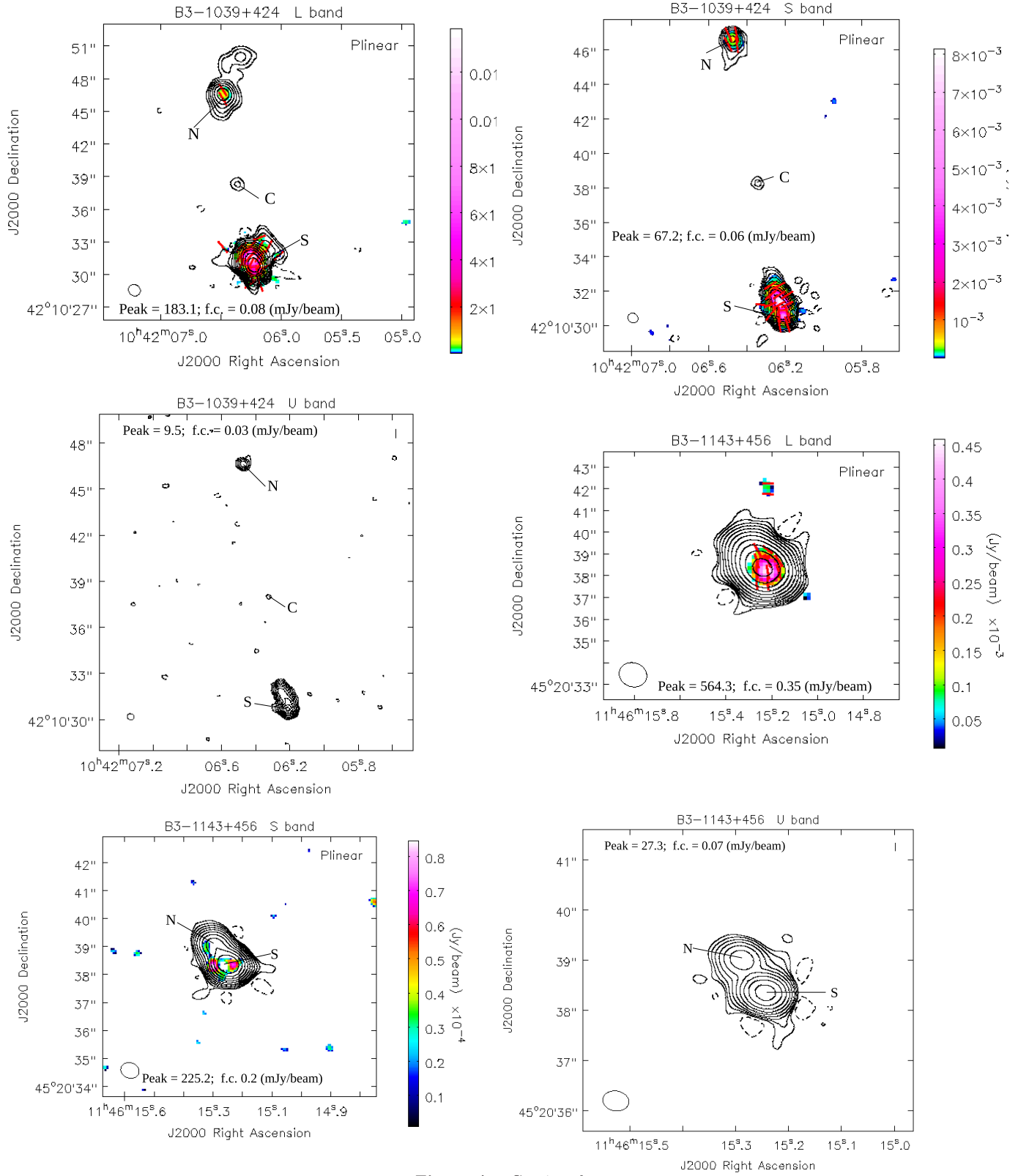


Figure A1. Continued.

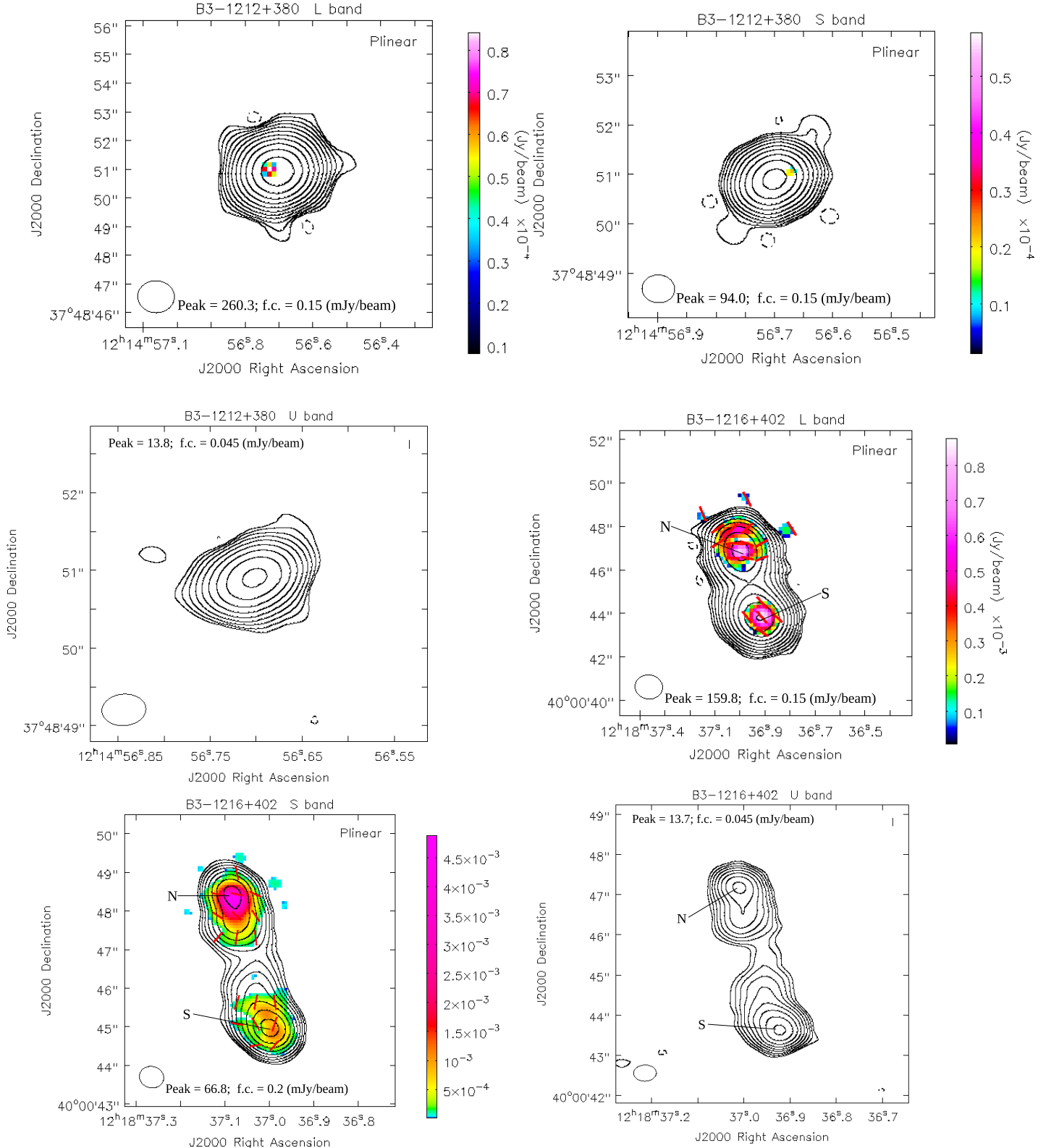


Figure A1. Continued.

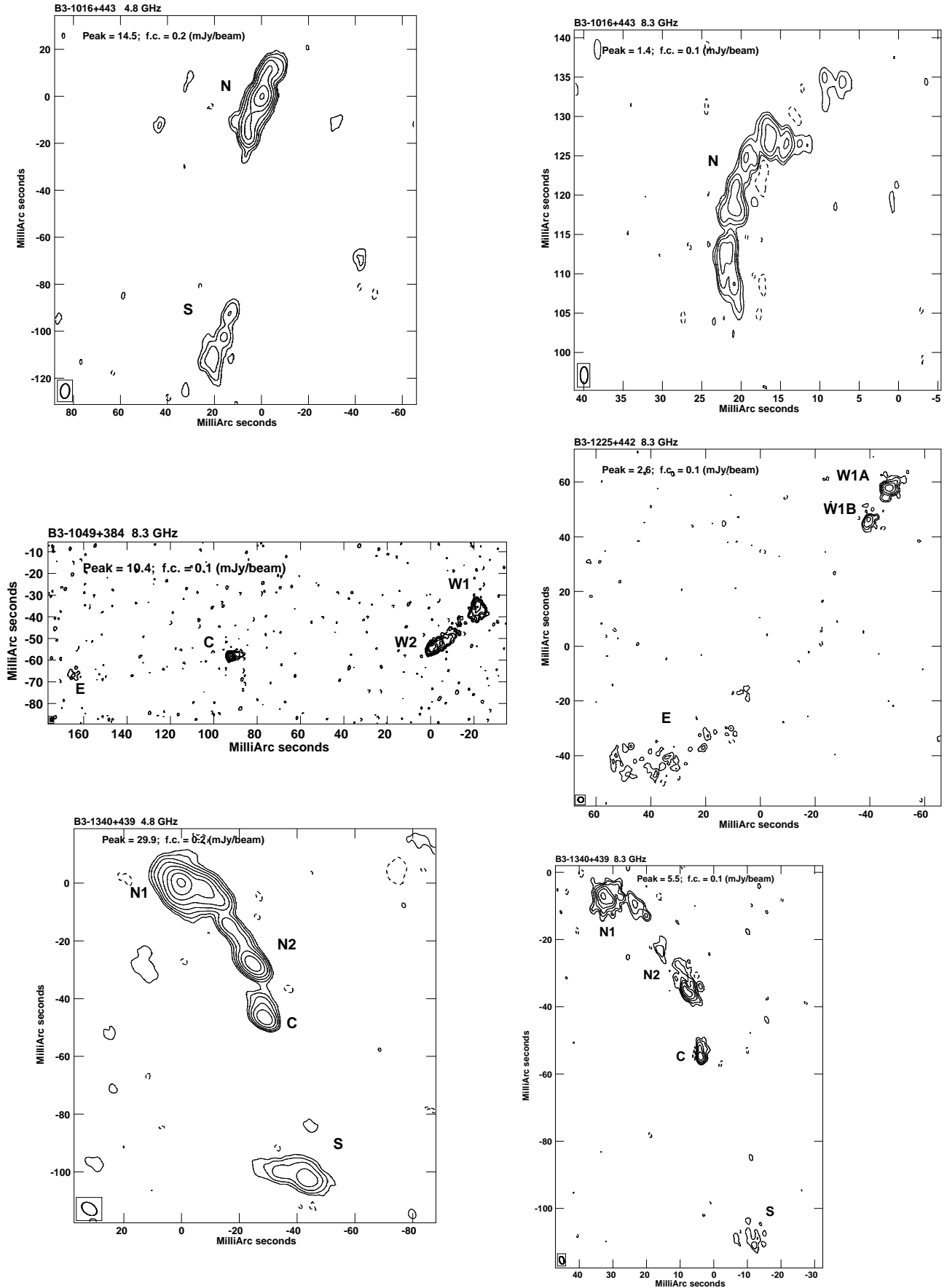


Figure A2. VLBA images of the CSS sources with LAS < 1 arcsec. On each image, we provide the source name, the observing band, the peak brightness (peak) and the first contour (f.c.), which is three times the off-source noise level on the image plane. Contours increase by a factor of 2. The beam is plotted in the bottom left-hand corner of each image.

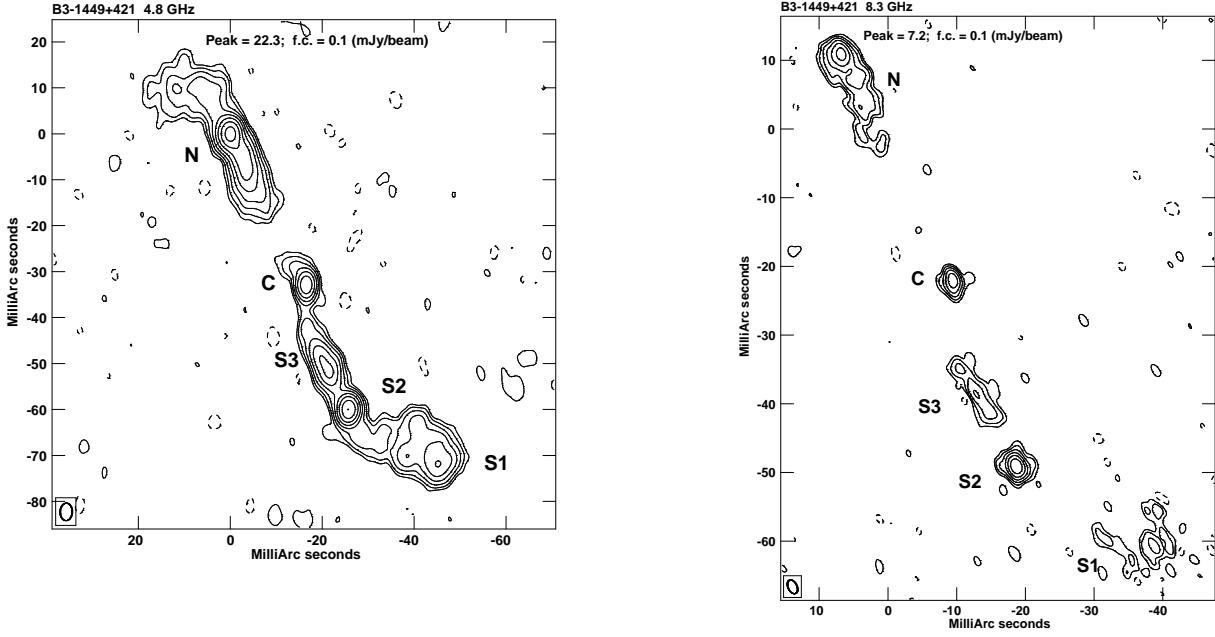


Figure A2. Continued.

Table B1. Flux density and morphology of the objects in the field of the target sources. Column 1: source name; columns 2 and 3: right ascension (RA) and declination (Dec); column 4: source component; column 5: flux density at 1.5 GHz; column 6: radio morphology. Cx: complex structure; CJ: core-jet, FRI: Fanaroff-Riley type-I radio source, FRII: Fanaroff-Riley type-II radio source, SR: slightly resolved, T: triple, U: unresolved.

Source name	RA (J2000)	Dec (J2000)	Component	Flux density mJy	Morph.
NVSS J000654+390200	00:06:54.54	39:02:00.34	Tot	9.7±0.4	FRII
			W	4.2±0.2	
			C	1.5±0.1	
			E	4.0±0.2	
B3-0004+387	00:07:30.34	39:03:47.0	Tot	42.5±1.3	U
NVSS J014352+385702	01:43:52.46	38:57:02.38	Tot	29.4±0.9	U
B3-0748+413A	07:51:45.16	41:15:35.93	Tot	180.3±5.5	Cx
FIRST J075255.6+410950	07:52:55.63	41:09:51.07	Tot	20.7±0.7	CJ?
			W	15.3±0.2	
			C	1.7±0.2	
			E	3.3±0.2	
B3-0754+394	07:58:00.06	39:20:29.20	Tot	11.3±0.4	U
FIRST J075803.0+392046	07:58:02.97	39:20:47.1	Tot	20.6±0.7	FRI?
NVSS J085935+401826	08:59:35.96	40:18:26.13		22.6±0.7	U
NVSS J104144+420746	10:41:44.00	42:07:46.08	Tot	9.9±0.3	T
			N	0.5±0.1	
			C	4.9±0.2	
			S	4.5±0.2	
NVSS J104134+420916	10:41:34.78	42:09:16.43	Tot	8.1±0.2	SR
WISEA J114540.82+452230.7	11:45:40.81	45:22:31.05	Tot	5.9±0.2	U

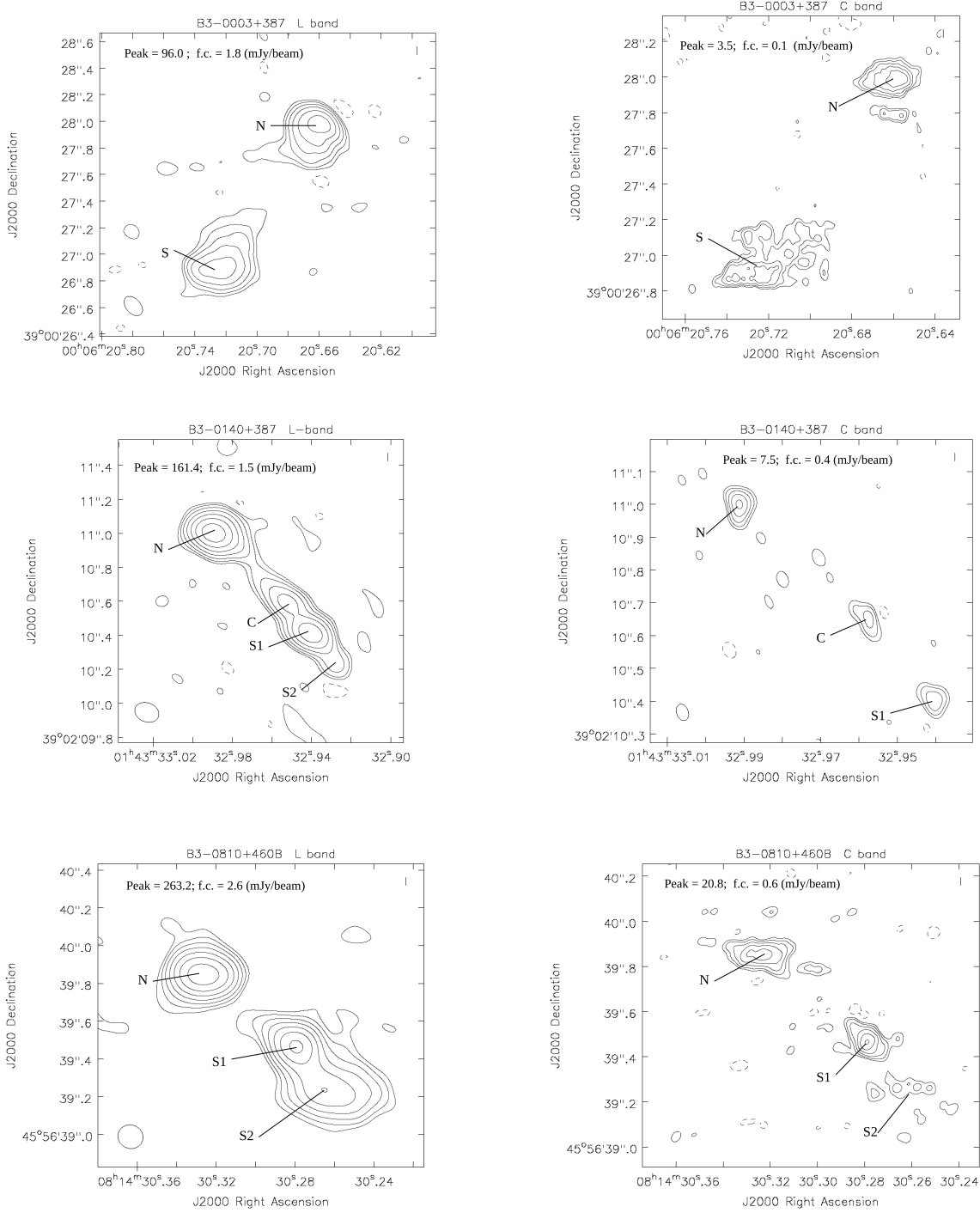


Figure A3. eMERLIN images of the CSS sources. On each image, we provide the source name, the observing band, the peak brightness (peak) and the first contour (f.c.), which is three times the off-source noise level on the image plane. Contours increase by a factor of 2. The beam is plotted in the bottom left-hand corner of each image.

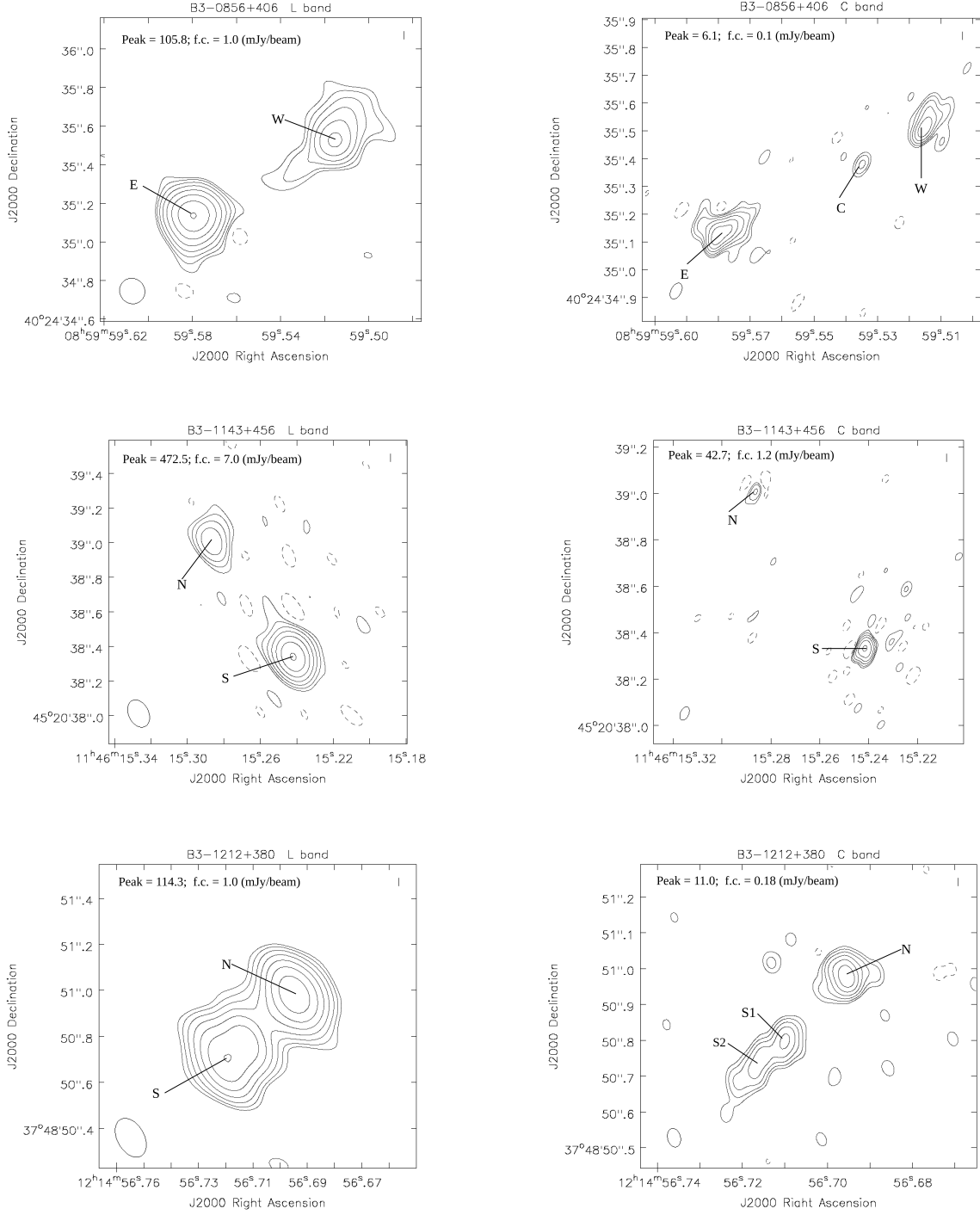


Figure A3. Continued.

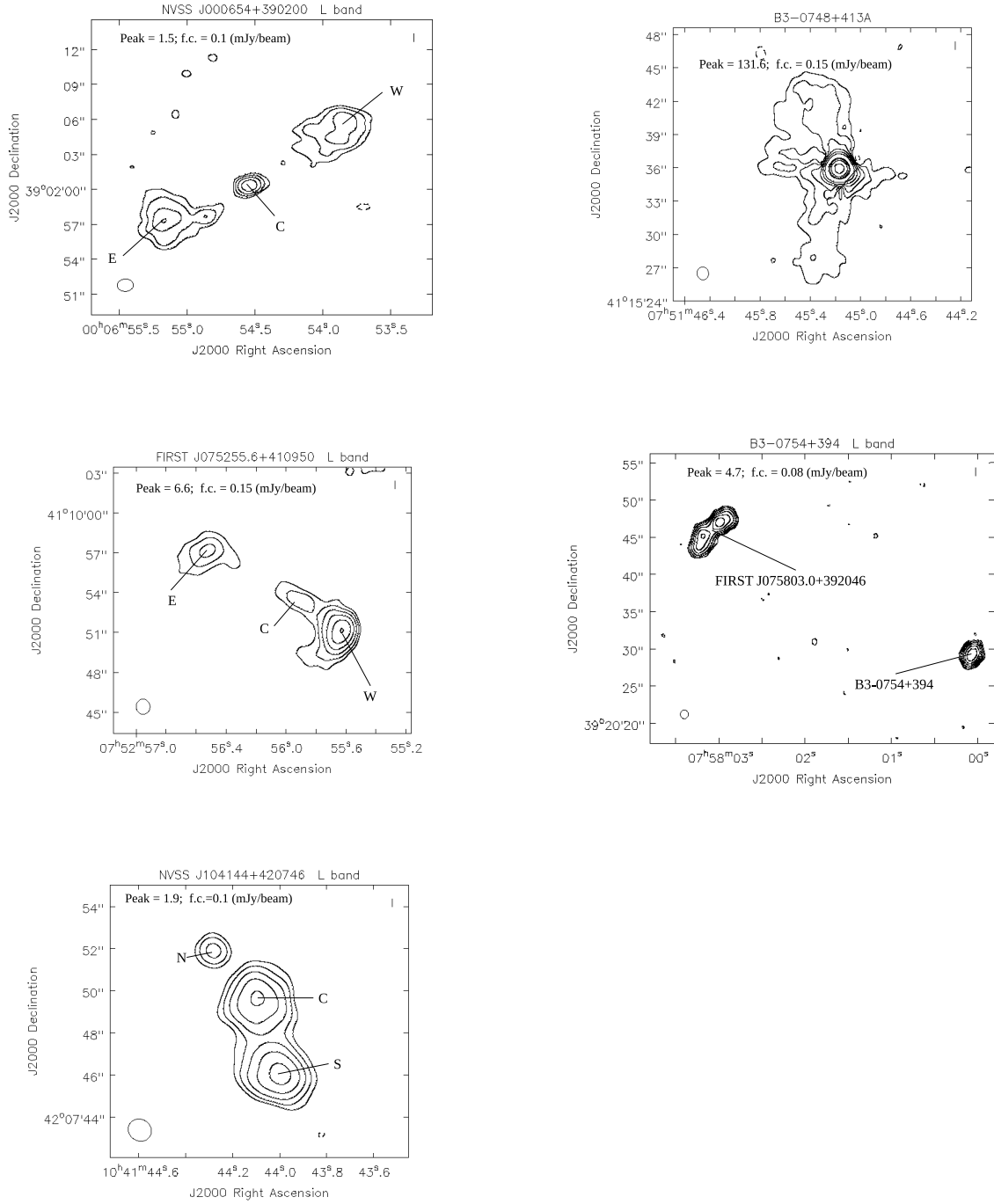


Figure B1. VLA images in L band of the objects with a resolved radio structure that fall within the field of view of the observations. On each image, we provide the source name, the observing band, the peak brightness (peak) and the first contour (f.c.), which is three times the off-source noise level on the image plane. Contours increase by a factor of 2. The beam is plotted in the bottom left-hand corner of each image.

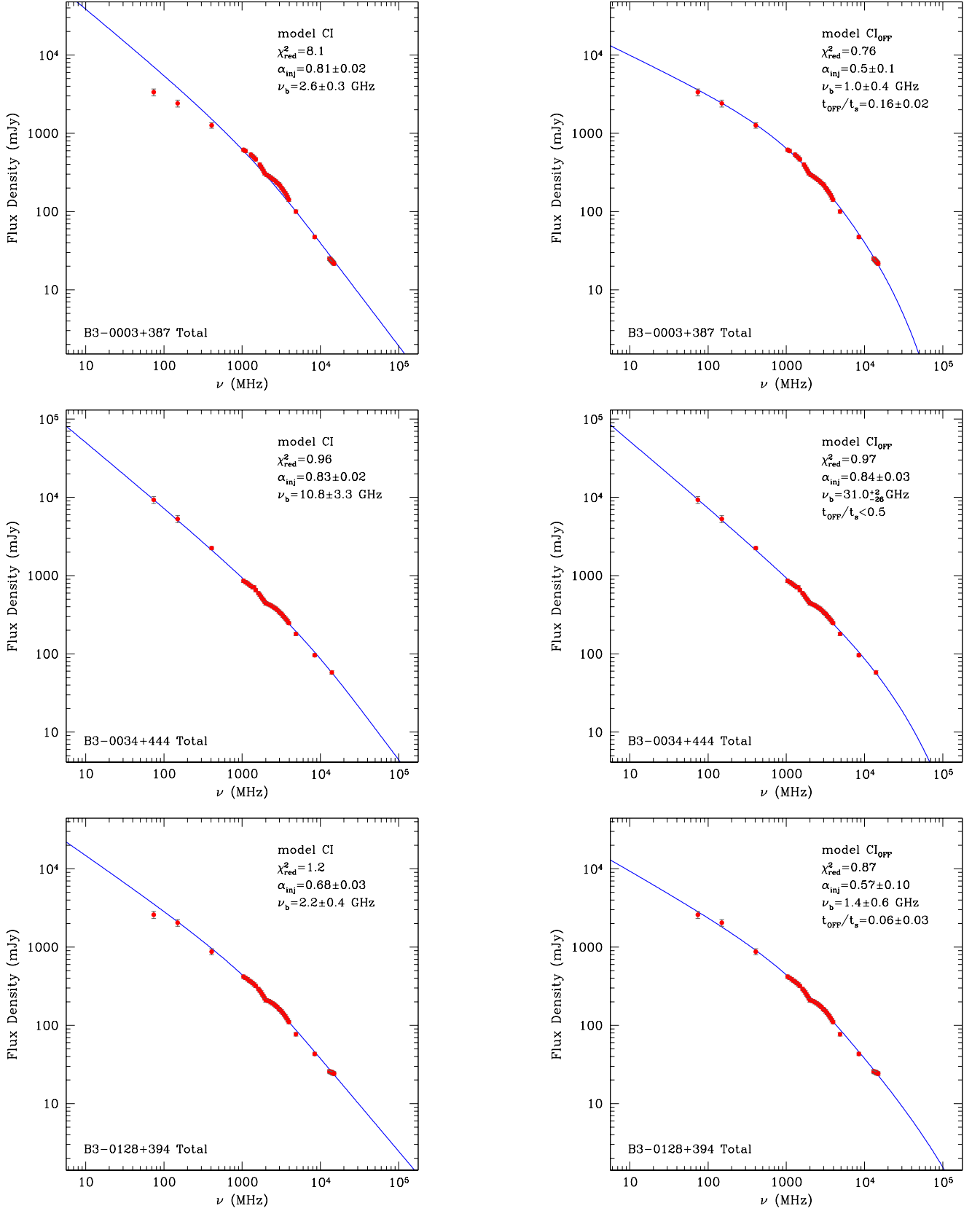


Figure C1. Integrated spectrum of the sources along with the best-fit CI model (*left*) and best-fit CI OFF model (*right*).

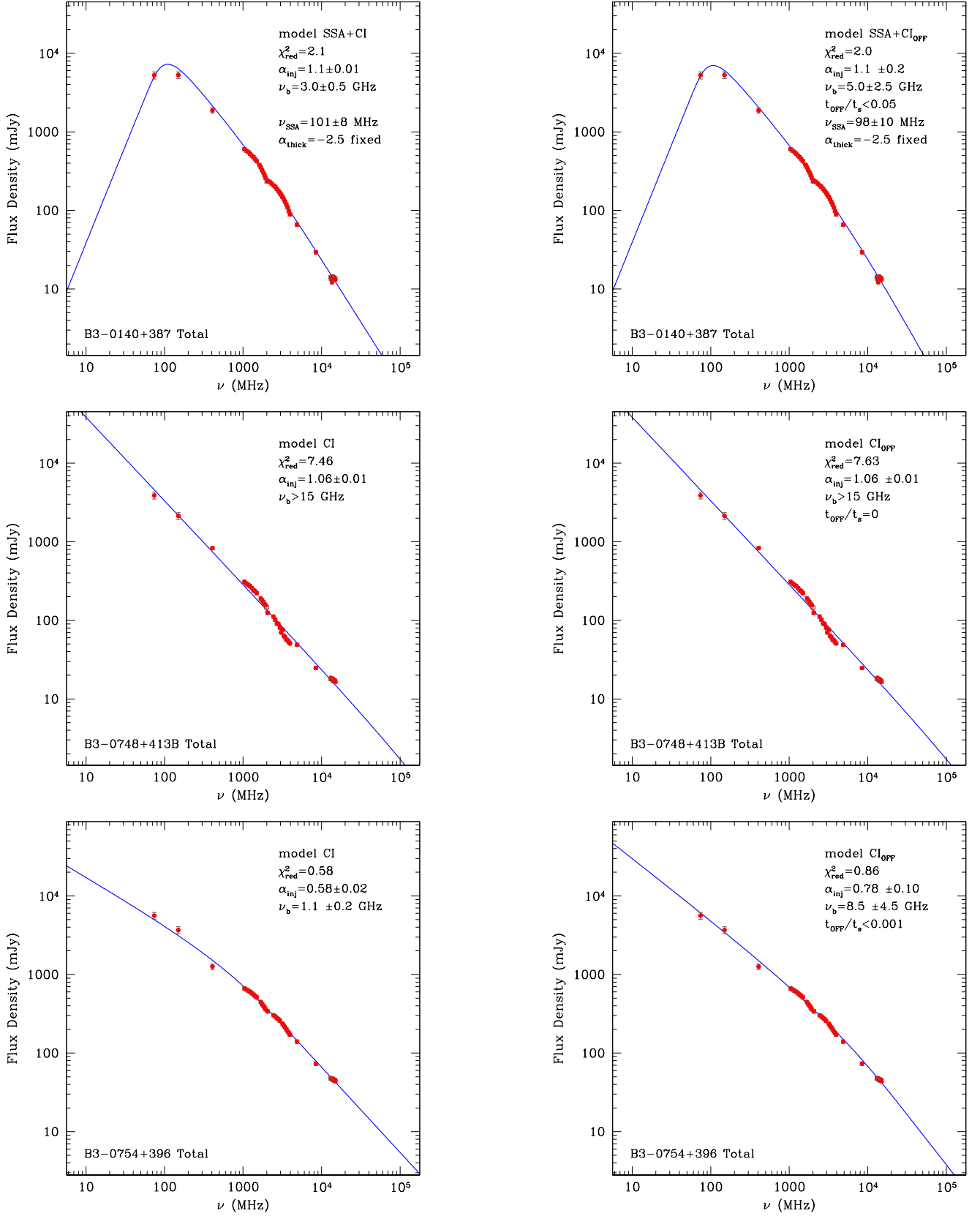


Figure C1. Continued.

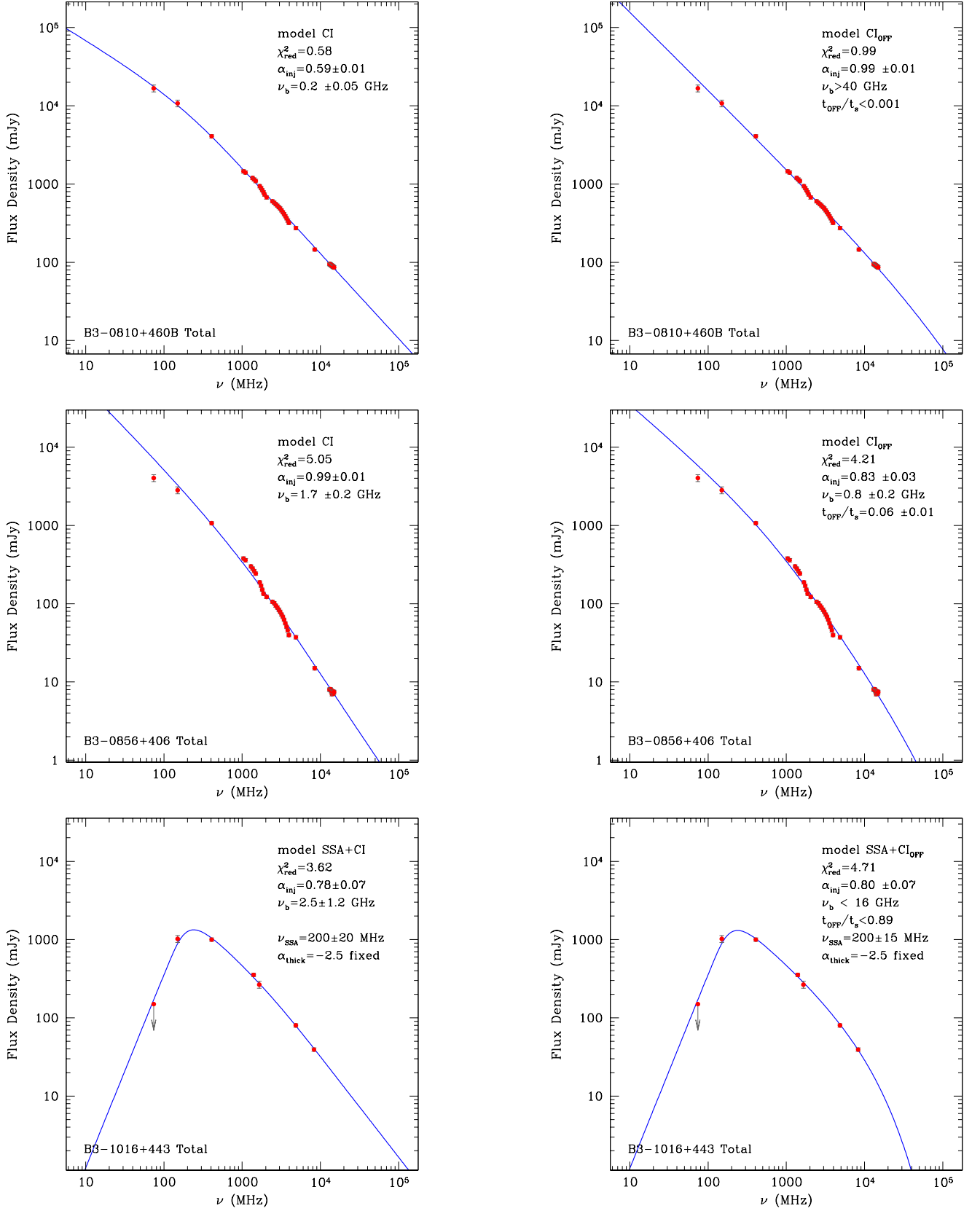


Figure C1. Continued.

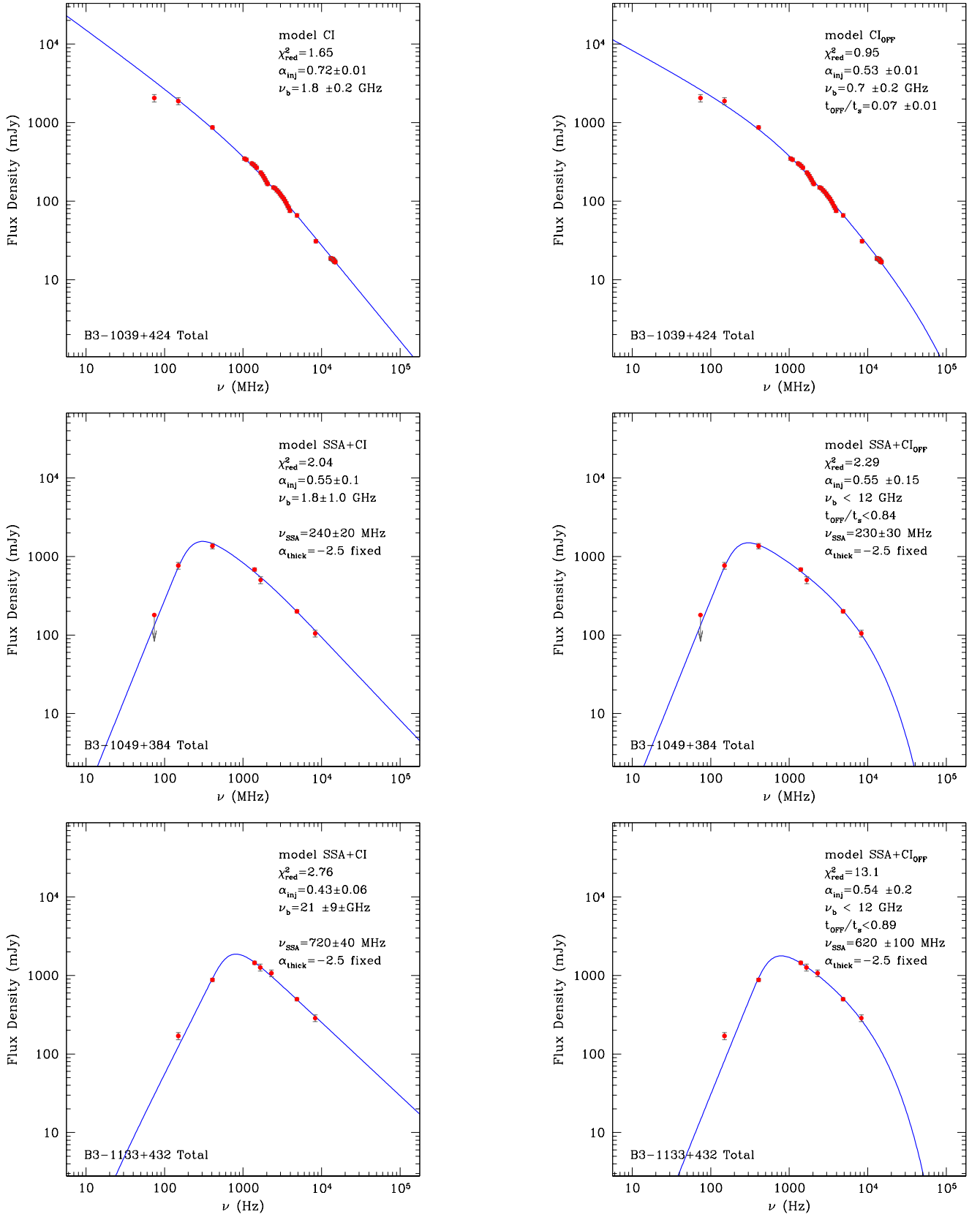


Figure C1. Continued.

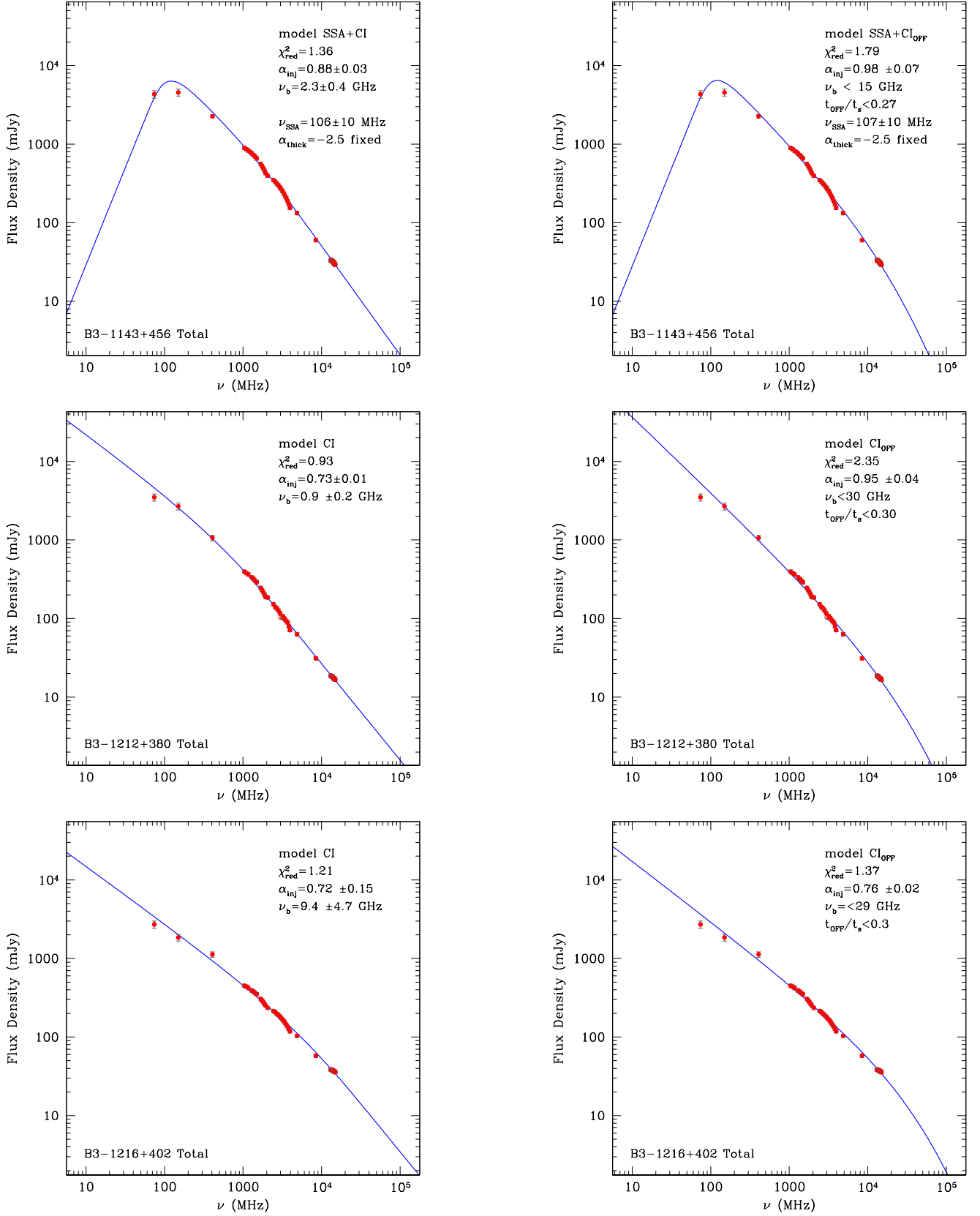


Figure C1. Continued.

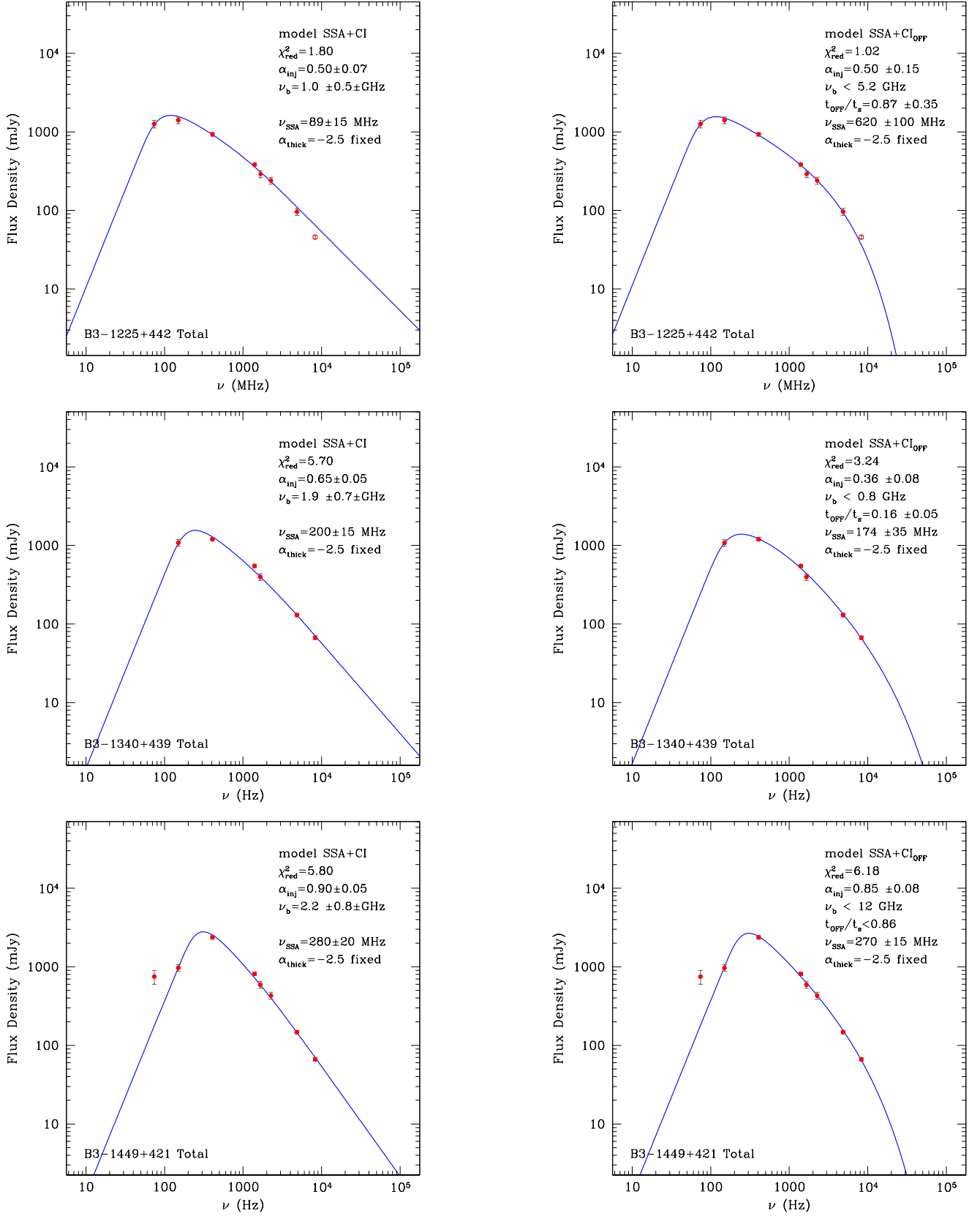


Figure C1. Continued.

Table C1. Best-fit parameters. Column 1: source name; columns 2, 3, 4, and 5: injection spectral index, break frequency, turnover frequency, reduced chi-square, respectively, for the CI model. Columns 6, 7, 8, 9, and 10: injection spectral index, break frequency, the relic to total source age ratio, turnover frequency, reduced chi-square, respectively, for the CI OFF model.

Source	CI				CI OFF				
	α_{inj}	ν_{b} GHz	ν_{SSA} MHz	χ^2_{red}	α_{inj}	ν_{b} GHz	$t_{\text{OFF}}/t_{\text{s}}$	ν_{SSA} MHz	χ^2_{red}
B3-0003+387	0.81±0.02	2.6±0.3	-	8.1	0.5±0.1	1.0±0.4	0.16±0.02	-	0.76
B3-0034+444	0.83±0.02	10.8±3.3	-	0.96	0.84±0.03	31 ⁺² ₋₂₆	<0.5	-	0.97
B3-0128+394	0.68±0.03	2.2±0.4	-	1.2	0.57±0.10	1.4±0.6	0.06±0.03	-	0.87
B3-0140+387	1.10±0.01	3.0±0.5	101±8	2.1	1.1±0.2	5.0±2.5	<0.05	98±10	2.0
B3-0748+413B	1.06±0.01	> 15	-	7.46	1.06±0.01	> 15	-	-	7.63
B3-0754+396	0.58±0.02	1.1±0.2	-	0.58	0.78±0.10	8.5±4.5	<0.001	-	0.86
B3-0810+460B	0.59±0.01	0.2±0.05	-	0.58	0.99±0.01	> 40	<0.001	-	0.99
B3-0856+406	0.99±0.01	1.7±0.2	-	5.05	0.83±0.03	0.8±0.2	0.06±0.01	-	4.21
B3-1016+443	0.78±0.07	2.5±1.2	200±20	3.62	0.80±0.07	<16	<0.89	200±15	4.71
B3-1039+424	0.72±0.01	1.8±0.2	-	1.65	0.53±0.01	0.7±0.2	0.07±0.01	-	0.95
B3-1049+384	0.55±0.10	1.8±1.0	240±20	2.04	0.55±0.15	<12	<0.84	230±30	2.29
B3-1133+432	0.43±0.06	21±9	720±40	2.76	0.54±0.20	<12	<0.89	620±100	13.1
B3-1143+456	0.88±0.03	2.3±0.4	106±10	1.36	0.98±0.07	<15	<0.27	107±10	1.79
B3-1212+380	0.73±0.01	0.9±0.2	-	0.93	0.95±0.04	<30	<0.30	-	2.35
B3-1216+402	0.72±0.15	9.4±4.7	-	1.21	0.76±0.02	<29	<0.3	-	1.37
B3-1225+442	0.50±0.07	1.0±0.5	89±15	1.80	0.50±0.15	<5.2	0.87±0.35	620±100	1.02
B3-1340+439	0.65±0.05	1.9±0.7	200±15	5.70	0.36±0.08	<0.8	0.16±0.05	174±35	3.24
B3-1449+421	0.90±0.05	2.2±0.8	280±20	5.80	0.85±0.08	<12	<0.86	270±15	6.18